APPENDIX A

The Joint Committee for Powder Diffraction Standards (JCPDS) [48]

ZnO, JCPDS file number 00-005-0664

Name and formula

Reference code:	00-005-0664
Mineral name:	Zincite, syn
Common name:	zinc white
PDF index name:	Zinc Oxide
Empirical formula:	OZn
Chemical formula:	ZnO

Crystallographic parameters

Crystal system:	Hexagonal
Space group:	P63mc
Space group number:	186
a (?):	3.2490
b (?):	3.2490
c (?):	5.2050
Alpha (?):	90.0000
Beta (?):	90.0000
Gamma (?):	120.0000
Calculated density (g/cm^3):	5.68
Measured density (g/cm^3):	5.66
Volume of cell (10^6 pm^3):	47.58
Z:	2.00
RIR:	4.50

Status, subfiles and quality

Subfiles:	Inorganic Mineral Alloy, metal or intermetalic Common Phase Forensic NBS pattern
Quality:	Indexed (I)

Comments

Color:	White
General comments:	Opaque mineral optical data on specimen from Sterling Hill, New Jersey, USA: R_3R%=11.8, Disp.=Std., VHN_{100}=190-219, Ref.: IMA Commission on Ore Microscopy QDF.
Sample source:	Sample from New Jersey Zinc Company, Sterling Hill, New Jersey, USA.
Analysis:	Spectroscopic analysis: <0.001% each of Mg, Si and Ca.
Optical data:	B=2.013, Q=2.029, Sign=+
Melting point:	1670(10)฀
Temperature:	X-ray pattern at 26 C.

References

Primary reference:	Swanson, Fuyat., *Natl. Bur. Stand. (U.S.), Circ. 539*, **2**, 25, (1953)
Optical data:	*Dana's System of Mineralogy, 7th Ed.*, **1**, 504

Peak list

No.	h	k	l	d [A]	2Theta[deg]	I [%]
1	1	0	0	2.81600	31.751	71.0
2	0	0	2	2.60200	34.440	56.0
3	1	0	1	2.47600	36.252	100.0
4	1	0	2	1.91100	47.543	29.0
5	1	1	0	1.62600	56.555	40.0
6	1	0	3	1.47700	62.870	35.0
7	2	0	0	1.40700	66.388	6.0
8	1	1	2	1.37900	67.917	28.0
9	2	0	1	1.35900	69.057	14.0

10	0	0	4	1.30100	72.610	3.0
11	2	0	2	1.23800	76.956	5.0
12	1	0	4	1.18120	81.405	3.0
13	2	0	3	1.09290	89.630	10.0
14	2	1	0	1.06390	92.777	4.0
15	2	1	1	1.04220	95.311	10.0
16	1	1	4	1.01580	98.632	5.0
17	2	1	2	0.98480	102.923	4.0
18	1	0	5	0.97640	104.169	7.0
19	2	0	4	0.95550	107.448	1.0
20	3	0	0	0.93820	110.378	4.0
21	2	1	3	0.90690	116.288	12.0
22	3	0	2	0.88260	121.562	6.0
23	0	0	6	0.86750	125.234	1.0
24	2	0	5	0.83690	133.975	6.0
25	1	0	6	0.82900	136.618	2.0
26	2	1	4	0.82370	138.511	2.0
27	2	2	0	0.81250	142.905	5.0

Stick Pattern

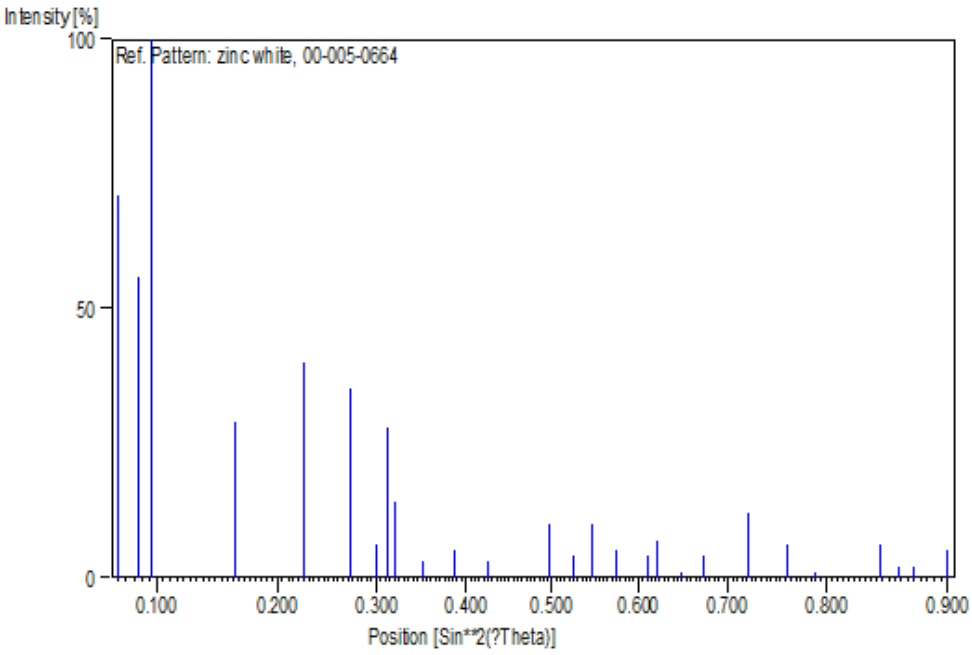

TiO_2, JCPDS file number 00-004-0477

Name and formula

Reference code:	00-004-0477
Mineral name:	Anatase, syn
PDF index name:	Titanium Oxide
Empirical formula:	O_2Ti
Chemical formula:	TiO_2

Crystallographic parameters

Crystal system:	Tetragonal
Space group:	I41/amd
Space group number:	141
a (?):	3.7830
b (?):	3.7830
c (?):	9.5100
Alpha (?):	90.0000
Beta (?):	90.0000
Gamma (?):	90.0000
Calculated density (g/cm^3):	3.90
Volume of cell (10^6 pm^3):	136.10
Z:	4.00
RIR:	-

Status, subfiles and quality

Subfiles:	Inorganic Mineral
Quality:	Indexed (I)

Comments

References

Primary reference: Swanson, Tatge., *Private Communication*, (1950)
Additional pattern: Parker., *Z. Kristallogr.*, **59**, 1, (1923)

Peak list

No.	h	k	l	d [A]	2Theta[deg]	I [%]
1	1	0	1	3.51000	25.354	100.0
2	1	0	3	2.43500	36.884	9.0
3	0	0	4	2.37900	37.785	22.0
4	1	1	2	2.33600	38.507	9.0
5	2	0	0	1.89100	48.077	33.0
6	1	0	5	1.69900	53.922	21.0
7	2	1	1	1.66500	55.116	19.0
8	2	1	3	1.49400	62.075	4.0
9	2	0	4	1.48000	62.728	13.0
10	1	1	6	1.36700	68.596	5.0
11	2	2	0	1.33700	70.359	5.0
12	2	1	5	1.26400	75.094	10.0
13	3	0	1	1.25000	76.084	3.0
14	3	0	3	1.17100	82.267	2.0
15	3	1	2	1.16090	83.140	3.0
16				1.08690	90.261	3.0
17	3	2	1	1.04330	95.179	3.0
18	1	0	9	1.01730	98.436	2.0
19	3	1	6	0.95500	107.530	4.0
20	4	0	0	0.94610	109.014	3.0
21	3	2	5	0.91890	113.919	2.0
22	1	1	10	0.89600	118.568	3.0
23	2	2	8	0.88770	120.396	2.0
24	3	2	7	0.83110	135.896	1.0
25	4	1	5	0.82680	137.391	3.0
26	3	0	9	0.81000	143.974	1.0
27				0.79900	149.193	3.0

Stick Pattern

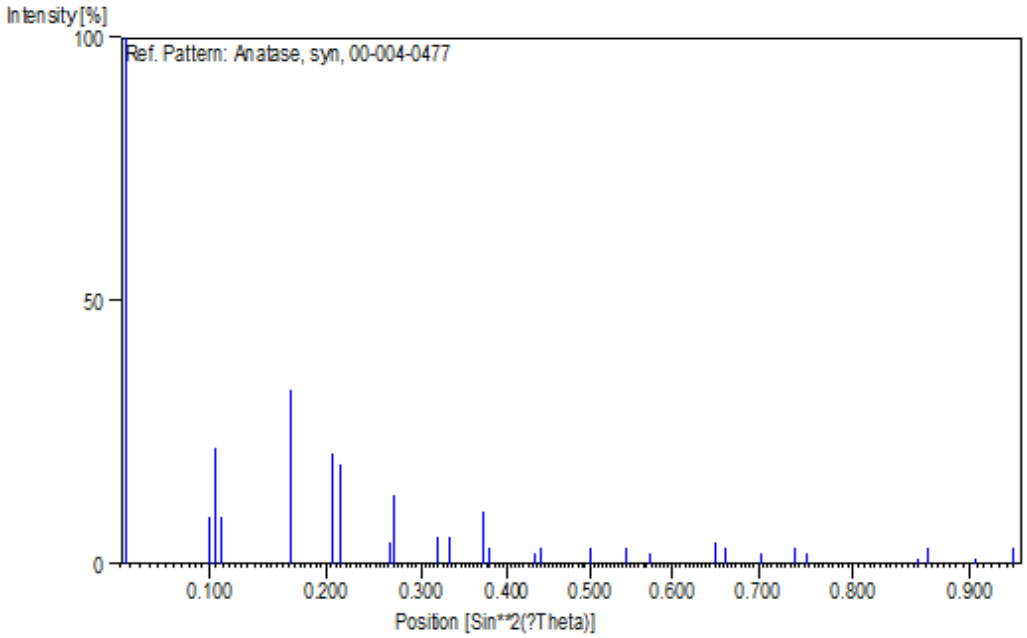

TiO_2, JCPDS file number 00-004-0551

Name and formula

Reference code:	00-004-0551
Mineral name:	Rutile
PDF index name:	Titanium Oxide
Empirical formula:	O_2Ti
Chemical formula:	TiO_2

Crystallographic parameters

Crystal system:	Tetragonal
Space group:	P42/mnm
Space group number:	136
a (?):	4.5940
b (?):	4.5940
c (?):	2.9580
Alpha (?):	90.0000
Beta (?):	90.0000
Gamma (?):	90.0000
Calculated density (g/cm^3):	4.25
Volume of cell (10^6 pm^3):	62.43
RIR:	-

Status, subfiles and quality

Subfiles:	Inorganic Mineral
Quality:	Indexed (I)

Comments

References

Primary reference: Swanson, Tatge, JC Fel. Reports, NBS., *Private*

Communication, (1950)

Peak list

No.	h	k	l	d [A]	2Theta[deg]	I [%]
1	1	1	0	3.24500	27.464	100.0
2	1	0	1	2.48900	36.056	41.0
3	2	0	0	2.29700	39.188	7.0
4	1	1	1	2.18800	41.226	22.0
5	2	1	0	2.05400	44.052	9.0
6	2	1	1	1.68700	54.337	50.0
7	2	2	0	1.62400	56.631	16.0
8	0	0	2	1.48000	62.728	8.0
9	3	1	0	1.45300	64.030	6.0
10	3	0	1	1.36000	68.999	16.0
11	1	1	2	1.34700	69.761	7.0
12	3	1	1	1.30500	72.352	1.0
13	2	0	2	1.24300	76.590	3.0
14	2	1	2	1.20000	79.870	1.0
15	3	2	1	1.17000	82.352	4.0
16	4	0	0	1.14850	84.242	4.0
17	4	1	0	1.11400	87.494	1.0
18	2	2	2	1.09330	89.589	4.0
19	3	3	0	1.08270	90.708	4.0
20	4	1	1	1.04240	95.287	5.0
21	3	1	2	1.03610	96.054	4.0
22	4	2	0	1.02730	97.151	3.0
23	1	0	3	0.96420	106.050	2.0
24	4	0	2	0.90710	116.247	3.0
25	5	1	0	0.90070	117.569	3.0
26	2	1	3	0.88920	120.059	5.0
27	4	3	1	0.87730	122.812	6.0
28	3	3	2	0.87390	123.636	5.0
29	4	2	2	0.84370	131.847	5.0
30	3	0	3	0.82900	136.618	5.0
31	5	2	1	0.81960	140.052	8.0

Stick Pattern

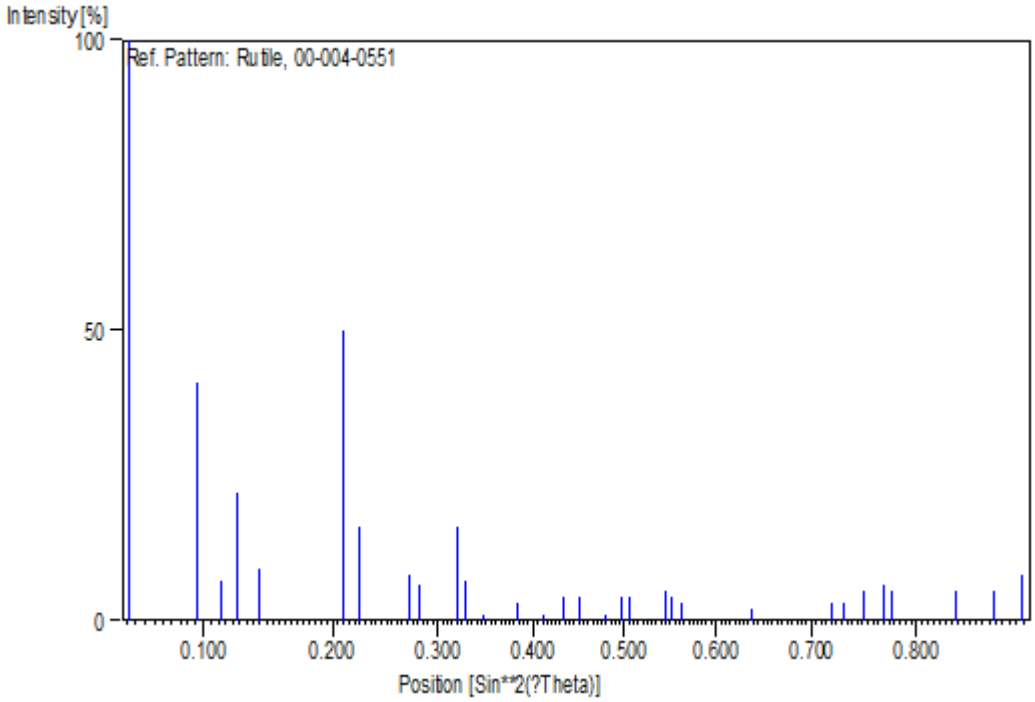

$ZnTiO_3$, JCPDS file number 00-026-1500

Name and formula

Reference code:	00-026-1500
Mineral name:	Ecandrewsite, syn
PDF index name:	Zinc Titanium Oxide
Empirical formula:	O_3TiZn
Chemical formula:	$ZnTiO_3$
Second chemical formula:	$ZnO . TiO_2$

Crystallographic parameters

Crystal system:	Rhombohedral
Space group:	R-3
Space group number:	148
a (?):	5.0787
b (?):	5.0787
c (?):	13.9270
Alpha (?):	90.0000
Beta (?):	90.0000
Gamma (?):	120.0000
Calculated density (g/cm^3):	5.16
Volume of cell (10^6 pm^3):	311.10
Z:	6.00
RIR:	2.50

Subfiles and Quality

Subfiles:	Inorganic Mineral Common Phase NBS pattern
Quality:	Star (S)

This is the quality mark distribution for 340,653 entries published in PDF-4+ Release 2013. Quality is defined by the ability to produce an accurate powder pattern with

known and consistent chemistry, physical properties, and unit cell parameters. The ICDD does over 100 separate checks in its quality review.
Star (S), Indexed (I), and Blank (B) marks are in decreasing order of quality. In these cases there is a unit cell and calculated d-spacings which can be compared to experimental d-spacings. Low precision data (O) tend to be historical in nature where d-spacings and intensities were visually estimated resulting in low precision. Rietveld (R) quality marks result from Rietveld refinements where there is a strong agreement with the structure and powder patterns resulting in high quality.

Calculated (C), Prototype (P) and Hypothetical Data (H) all result from calculation *and do not have corresponding experimental data*. The quality of these data are more difficult to ascertain. The user should be cautious using these data.

Comments

Color:	Colorless
General comments:	Because of the presence of small amounts of TiO_2 and Zn_2TiO_4 the intensities may have slight errors.
Sample preparation:	Prepared by heating an equimolar mixture of $Zn(NO_3)_2$ and TiO_2 (anatase) for two weeks at 900 C with remixings and reheatings.
Additional pattern:	To replace 25-671.
Temperature:	Pattern taken at 25 C.

References

Primary reference: *Natl. Bur. Stand. (U.S.) Monogr. 25*, **13**, 49, (1976)

Peak list

No.	h	k	l	d [A]	2Theta[deg]	I [%]
1	0	0	3	4.63000	19.154	1.0
2	1	0	1	4.19100	21.182	3.0
3	0	1	2	3.71700	23.921	20.0
4	1	0	4	2.72900	32.791	100.0
5	1	1	0	2.54000	35.308	75.0
6	0	1	5	2.35500	38.185	1.0
7	0	0	6	2.32100	38.766	1.0
8	1	1	3	2.22800	40.453	20.0
9	0	2	1	2.17300	41.524	3.0

10	2	0	2	2.09700	43.103	1.0
11	0	2	4	1.86000	48.930	35.0
12	1	0	7	1.81300	50.286	1.0
13	1	1	6	1.71300	53.446	35.0
14	2	1	1	1.65100	55.623	1.0
15	0	1	8	1.61900	56.821	11.0
16	2	1	4	1.50000	61.799	25.0
17	3	0	0	1.46600	63.396	25.0
18	1	2	5	1.42800	65.289	1.0
19	3	0	3	1.39900	66.817	1.0
20	2	0	8	1.36500	68.710	4.0
21	1	0	10	1.32760	70.932	8.0
22	1	1	9	1.32180	71.291	4.0
23	2	1	7	1.27600	74.268	1.0
24	2	2	0	1.26960	74.706	6.0
25	3	0	6	1.23960	76.838	2.0
26	0	1	11	1.21660	78.567	1.0
27	1	2	8	1.20200	79.710	6.0
28	0	2	10	1.17660	81.791	3.0
29	1	3	4	1.15120	84.000	7.0
30	2	2	6	1.11390	87.503	5.0
31	0	4	2	1.08620	90.335	1.0
32	2	1	10	1.06740	92.383	5.0
33	1	1	12	1.05580	93.704	2.0
34	4	0	4	1.04850	94.558	3.0
35	1	2	11	1.00690	99.818	1.0
36	3	1	8	0.99900	100.900	3.0
37	2	2	9	0.98160	103.393	1.0
38	0	1	14	0.97020	105.114	4.0
39	3	2	4	0.96920	105.269	7.0
40	4	1	0	0.95990	106.735	5.0
41	0	4	8	0.92960	111.918	2.0
42	1	3	10	0.91750	114.188	3.0
43	2	0	14	0.90640	116.390	2.0
44	4	1	6	0.88680	120.599	5.0

Stick Pattern

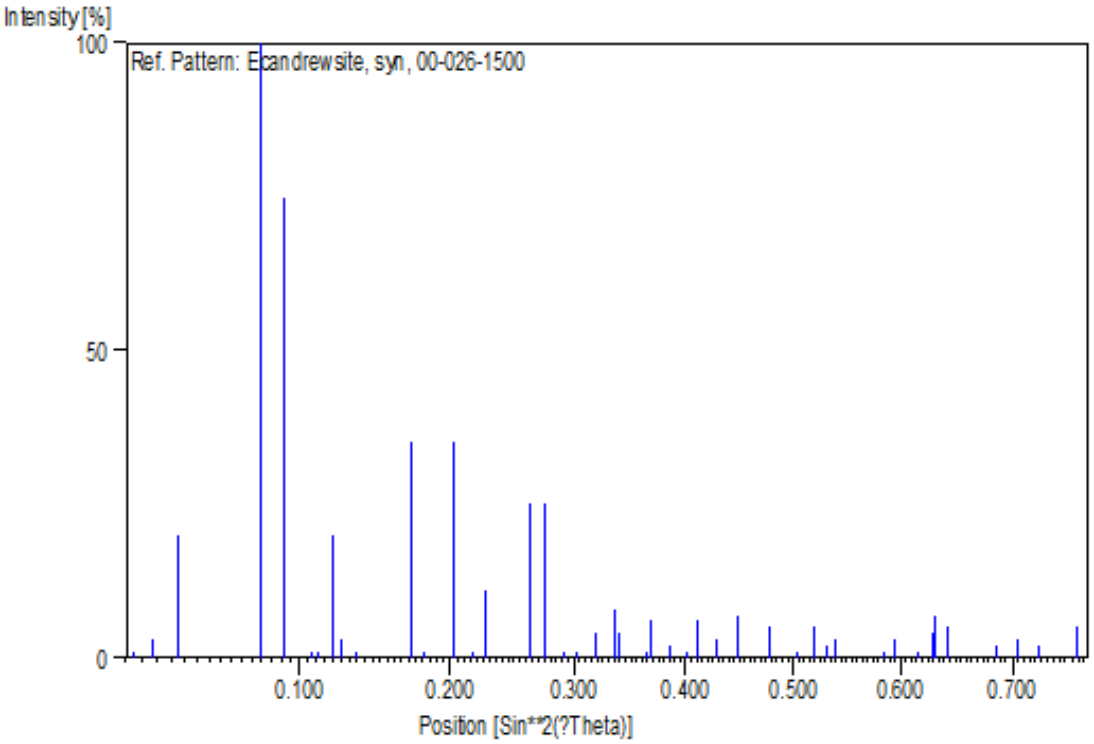

$Zn2TiO_4$, JCPDS file number 00-019-1483

Name and formula

Reference code:	00-019-1483
PDF index name:	Zinc Titanium Oxide
Empirical formula:	O_4TiZn_2
Chemical formula:	Zn_2TiO_4

Crystallographic parameters

Crystal system:	Tetragonal
a (?):	6.0050
b (?):	6.0050
c (?):	8.4160
Alpha (?):	90.0000
Beta (?):	90.0000
Gamma (?):	90.0000
Volume of cell (10^6 pm^3):	303.48
Z:	4.00
RIR:	-

Subfiles and Quality

Subfiles:	Inorganic
Quality:	Doubtful (O)

Comments

General comments:	Transforms to cubic modification above 770 C.

References

Primary reference:	Vincent, Joubert, Durif., *Bull. Soc. Chim. Fr.*, 246, (1966)

Peak list

No.	h	k	l	d [A]	2Theta[deg]	I [%]
1	1	0	0	5.96000	14.852	2.0
2	1	0	1	4.87000	18.202	8.0
3	1	1	1	3.78000	23.517	2.0
4	2	0	0	3.00000	29.757	20.0
5	1	1	2	2.99000	29.858	35.0
6	1	0	3	2.55000	35.165	100.0
7				2.53000	35.452	50.0
8	2	0	2	2.44000	36.806	10.0
9	1	1	3	2.34000	38.439	2.0
10	2	1	2	2.25000	40.041	2.0
11	2	2	0	2.12000	42.612	18.0
12	0	0	4	2.10000	43.038	10.0
13	3	0	2	1.81700	50.167	2.0
14				1.80500	50.524	2.0
15	3	1	2	1.72900	52.913	14.0
16	2	0	4	1.72000	53.212	8.0
17	3	2	1	1.63200	56.328	30.0
18	3	0	3	1.62700	56.517	14.0
19	1	0	5	1.61900	56.821	14.0
20	3	1	3	1.57100	58.724	2.0
21	3	2	2	1.54600	59.769	2.0
22	4	0	0	1.50000	61.799	25.0
23	2	2	4	1.49300	62.121	45.0

Stick Pattern

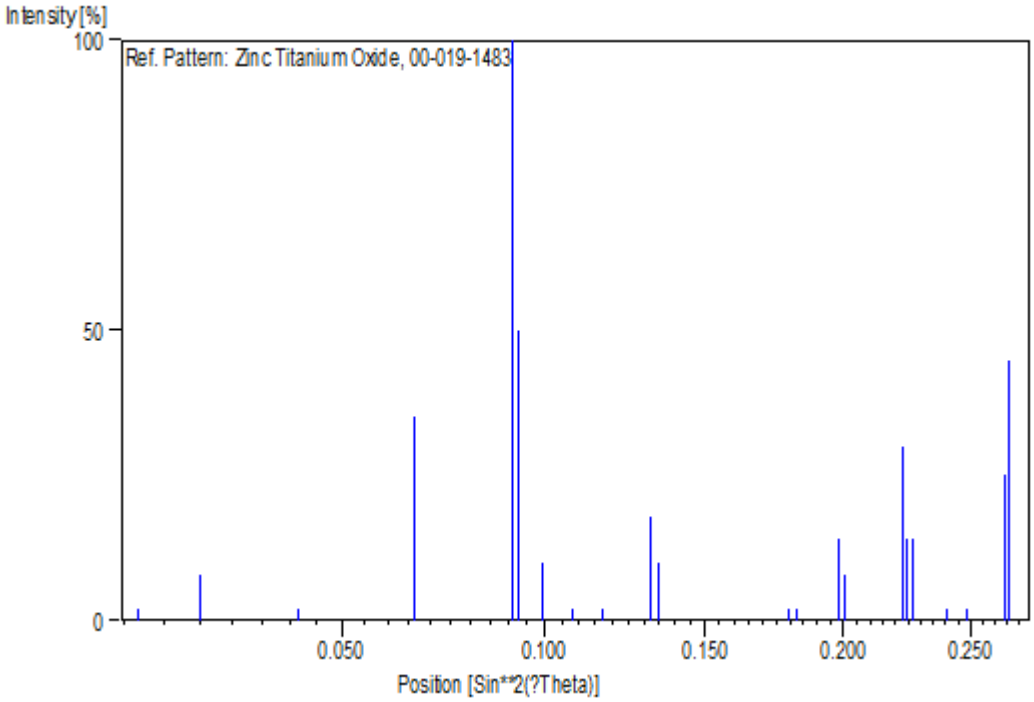

$Zn_2Ti_3O_8$, JCPDS file number 01-073-0579

Name and formula

Reference code:	01-073-0579
ICSD name:	Zinc Titanium Oxide
Empirical formula:	$O_8Ti_3Zn_2$
Chemical formula:	$Zn_2Ti_3O_8$

Crystallographic parameters

Crystal system:	Cubic
Space group:	Fd3m
Space group number:	227
a (?):	8.3950
b (?):	8.3950
c (?):	8.3950
Alpha (?):	90.0000
Beta (?):	90.0000
Gamma (?):	90.0000
Calculated density (g/cm^3):	4.52
Measured density (g/cm^3):	4.61
Volume of cell (10^6 pm^3):	591.65
Z:	4.00
RIR:	4.23

Subfiles and Quality

Subfiles:	Inorganic Corrosion Modelled additional pattern
Quality:	Calculated (C)

This is the quality mark distribution for 340,653 entries published in PDF-4+ Release 2013. Quality is defined by the ability to produce an accurate powder pattern with known and consistent chemistry, physical properties, and unit cell parameters. The ICDD does over 100 separate checks in its quality review.

Star (S), Indexed (I), and Blank (B) marks are in decreasing order of quality. In these cases there is a unit cell and calculated d-spacings which can be compared to experimental d-spacings. Low precision data (O) tend to be historical in nature where d-spacings and intensities were visually estimated resulting in low precision. Rietveld (R) quality marks result from Rietveld refinements where there is a strong agreement with the structure and powder patterns resulting in high quality.

Calculated (C), Prototype (P) and Hypothetical Data (H) all result from calculation *and do not have corresponding experimental data*. The quality of these data are more difficult to ascertain. The user should be cautious using these data.

Comments

ICSD collection code: 022381
Test from ICSD: Calc. density unusual but tolerable.
No R value given.

References

Primary reference: *Calculated from ICSD using POWD-12++*, (1997)
Structure: Bartram, S.F., Slepetys, A., *J. Am. Ceram. Soc.*, **44**, 493, (1961)

Peak list

No.	h	k	l	d [A]	2Theta[deg]	I [%]
1	1	1	1	4.84686	18.289	0.3
2	2	2	0	2.96808	30.084	58.7
3	3	1	1	2.53119	35.435	100.0
4	2	2	2	2.42343	37.067	0.6
5	4	0	0	2.09875	43.065	8.6
6	3	3	1	1.92595	47.151	3.2
7	4	2	2	1.71362	53.425	16.5
8	5	1	1	1.61562	56.951	32.8
9	4	4	0	1.48404	62.538	37.2
10	5	3	1	1.41901	65.755	0.2
11	4	4	2	1.39917	66.808	0.1
12	6	2	0	1.32737	70.946	5.2
13	5	3	3	1.28023	73.982	7.3
14	6	2	2	1.26559	74.984	0.7

15	4	4	4	1.21171	78.946	0.7
16	7	1	1	1.17554	81.881	0.4
17	6	4	2	1.12183	86.730	6.0
18	7	3	1	1.09294	89.626	9.8

Stick Pattern

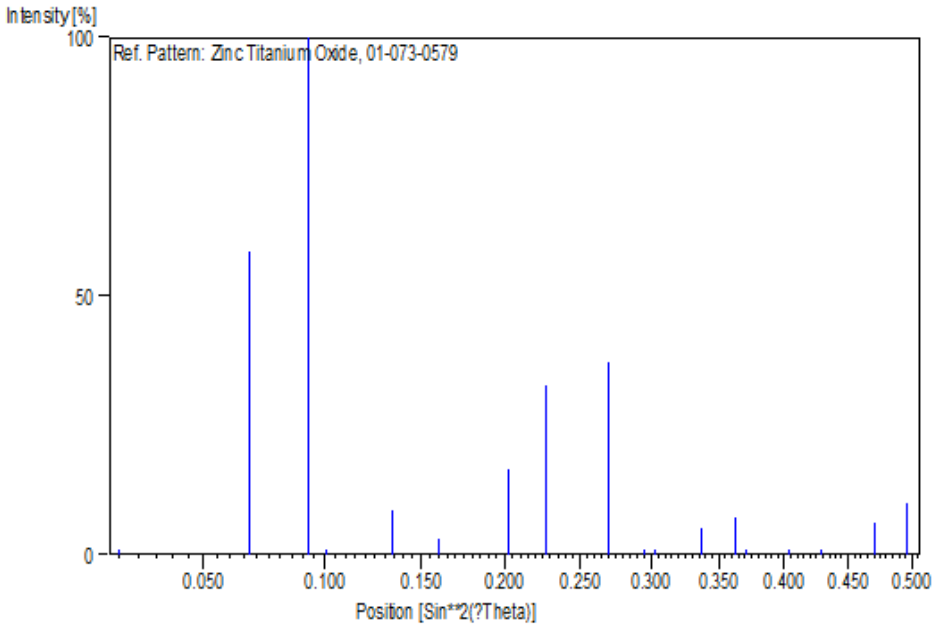

APPENDIX B

PUBLICATIONS

Materials Letters 96 (2013) 78–81

Contents lists available at SciVerse ScienceDirect

Materials Letters

journal homepage: www.elsevier.com/locate/matlet

Single-step synthesis of ZnO/TiO_2 nanocomposites by microwave radiation and their photocatalytic activities

Jirapong Arin [a], Somchai Thongtem [b,c], Titipun Thongtem [a,c,*]

[a] Department of Chemistry, Faculty of Science, Chiang Mai University, Chiang Mai 50200, Thailand
[b] Department of Physics and Materials Science, Faculty of Science, Chiang Mai University, Chiang Mai 50200, Thailand
[c] Materials Science Research Center, Faculty of Science, Chiang Mai University, Chiang Mai 50200, Thailand

ARTICLE INFO

Article history:
Received 29 October 2012
Accepted 9 January 2013
Available online 20 January 2013

Keywords:
Electron microscopy
Nanocomposites
Spectroscopy
X-ray techniques

ABSTRACT

$Zn(NO_3)_2 \cdot 6H_2O$ and $C_4K_2O_9Ti \cdot 2H_2O$ with 1:1 and 2:1 M ratios of Zn:Ti in solutions at the pH 10 were irradiated by 180 W microwave radiation for 40 min to form ZnO/TiO_2 nanocomposites, new candidates for photodegradation and photoreduction in UV light with very high efficiency. Upon processing the nanocomposites at high temperatures, pure Zn_2TiO_4 nanocrystals were synthesized only by the 700 °C and 3 h calcination of the 2:1 M ratio Zn:Ti precursors.

1. Introduction

Recently, photocatalytic materials have been intensively studied due to their high activities for hydrogen evolution from water, degradation of pollutants, CO_2 remediation, self-cleaning activity and air purification. Among them, TiO_2 is a good candidate for environmental remedy due to its non-toxic properties, biological and chemical stabilities, strong oxidizer, low cost and long-term stability against corrosion. Its photocatalysis is limited only in the UV range, including fast recombination of electron–hole pairs [1–3]. In order to enhance TiO_2 photocatalytic activities, it is considered to be put together with ZnO which is non-toxic, low cost, easy to be synthesized and wide application [4–7].

In this research, ZnO/TiO_2 nanocomposites were successfully synthesized by a single-step method using microwave radiation (MWR), and were further calcined at high temperature to form Zn_2TiO_4 single phase.

2. Experiment

Zinc nitrate hexahydrate ($Zn(NO_3)_2 \cdot 6H_2O$, 0.100 mol) was dissolved in 100 ml de-ionized water to form solution with the pH was adjusted to 10 using NH_4OH. Then 0.100 mol potassium titanium oxalate dihydrate ($C_4K_2O_9Ti \cdot 2H_2O$) in 100 ml de-ionized water as a whole was slowly added, with keeping the pH 10 throughout the process. The final solution was irradiated with 180 W MWR for two batches ($2 \times 20 = 40$ min) to form precipitates, which were separated, rinsed and dried at 70 °C for 36 h. Another product was synthesized as the above but 0.200 mol $Zn(NO_3)_2 \cdot 6H_2O$ was used. The products with 1:1 and 2:1 M ratios of Zn:Ti were labeled Anon and Bnon, respectively. They were further calcined at 500, 600 and 700 °C for 3 h, and labeled A500, A600 and A700 for the first and B500, B600 and B700 for the second.

To study photodegradation, 70 ml 5×10^{-6} M methylene blue (MB) solutions with and without adding each of 1.00 g product were stirred for 1 h in the dark environment to stabilize them, and irradiated with two 18 W UV lamps for 0–150 min. The MB solution without adding of the photocatalytic product was labeled Blank. Decolorization efficiency was calculated at 671 nm wavelength. Similarly, photoreduction of $K_2Cr_2O_7$ was at 345 nm.

3. Results and discussion

XRD patterns (Fig. 1) of different products were compared with the JCPDS database nos. 00-005-0664 (hexagonal ZnO), 00-004-0477 (TiO_2, tetragonal anatase), 01-077-0014 (cubic Zn_2TiO_4) and 00-039-0190 (cubic $ZnTiO_3$) [8]. Both ZnO/TiO_2 composites of Anon and Bnon were successfully synthesized by the MWR process. The synthesis of Zn_2TiO_4 single phase was success only by the 700 °C and 3 h calcination of the Bnon. All ZnO and TiO_2 precursors were chemically combined to form pure Zn_2TiO_4

* Corresponding author at: Department of Chemistry, Faculty of Science, Chiang Mai University, Chiang Mai 50200, Thailand. Tel.: +66 53 943344; fax: +66 53 892277.
E-mail addresses: ttpthongtem@yahoo.com, ttpthongtem@gmail.com (T. Thongtem).

0167-577X/$ - see front matter © 2013 Elsevier B.V. All rights reserved.
http://dx.doi.org/10.1016/j.matlet.2013.01.026

without residual detection. For B500 and B600, $ZnTiO_3$ and Zn_2TiO_4 were synthesized, with TiO_2 remains. In this research, A500, A600 and A700 were still to be mixtures of different phases although the calcination temperature was as high as 700 °C.

At the beginning, $Zn(NO_3)_2 \cdot 6H_2O$ and $C_4K_2O_9Ti \cdot 2H_2O$ formed complexes ions in the solutions at the pH 10.

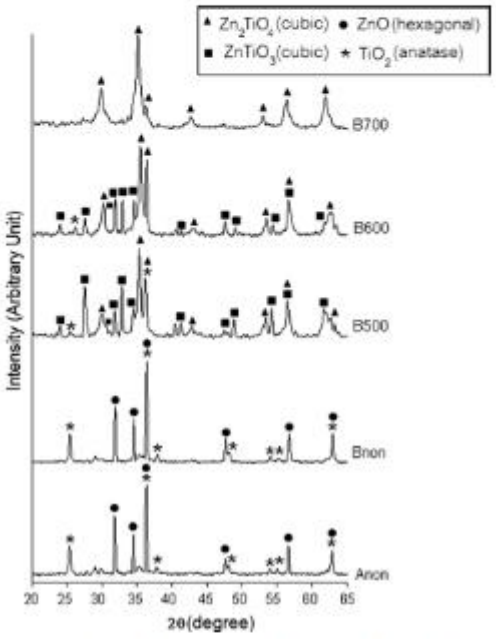

Fig. 1. XRD patterns of Anon, Bnon, B500, B600 and B700.

$Zn(NO_3)_2 \cdot 6H_2O + NH_4OH \rightarrow$ Zn-complexes ions

$C_4K_2O_9Ti \cdot 2H_2O + NH_4OH \rightarrow$ Ti-complexes ions

They were processed by MWR to form composites.

Zn-complexes ions + Ti-complexes ions $\rightarrow ZnO/TiO_2$ composites

Upon calcination at 500, 600 and 700 °C, different products were synthesized.

$ZnO + TiO_2 \rightarrow ZnTiO_3$

$2ZnO + TiO_2 \rightarrow Zn_2TiO_4$

A number of nanoparticles with different orientations in space were characterized by EM. Before calcination, Bnon (Figs. 2a and 3a) was composed of very tiny particles with < 10 nm. At 500 °C calcination (Figs. 2b and 3c, d), these nanoparticles grew up with the presence of faces and angles, specified as crystals. Further increasing the calcination temperature to 600 °C (Fig. 2c) and 700 °C (Figs. 2d and 3e), the products respectively became 25 nm and 80–100 nm nanocrystals with smooth surfaces. A SAED pattern of Bnon (Fig. 3b) presents bright concentric rings, diffracted from very tiny particles with different orientations, and specified as ZnO/TiO_2 nanocomposites [8]. At 700 °C calcination (Fig. 3f), the pattern was still concentric rings but diffraction spots were moved apart—suggested to be diffracted from a number of better crystals with different orientations, corresponding to Zn_2TiO_4 [8].

Decolorization efficiency (Fig. 4a) of MB in the solutions containing Anon and Bnon exhibited much higher photocatalytic activities than those of the B700 and Blank solutions. B500 and B600 were mixtures of $ZnTiO_3$, Zn_2TiO_4 (deficiency in photocatalysis) and TiO_2, thus they were not appropriate for studying. Photodegradation of MB in the Anon and Bnon solutions was much the same performance and continuously increased with the lengths of time. As 150 min passed, decolorization efficiencies of both were very close to 100%. The higher photoactivity was enhanced by the higher electron–hole separation rate and the formation of p–n junctions of the ZnO/TiO_2 nanocomposites [3,9]. The photogenerated electrons could easily diffuse from the inner

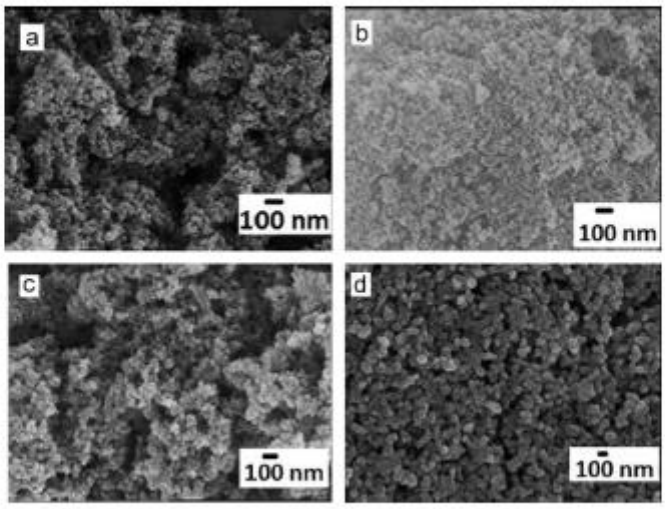

Fig. 2. SEM images of (a–d) Bnon, B500, B600 and B700, respectively.

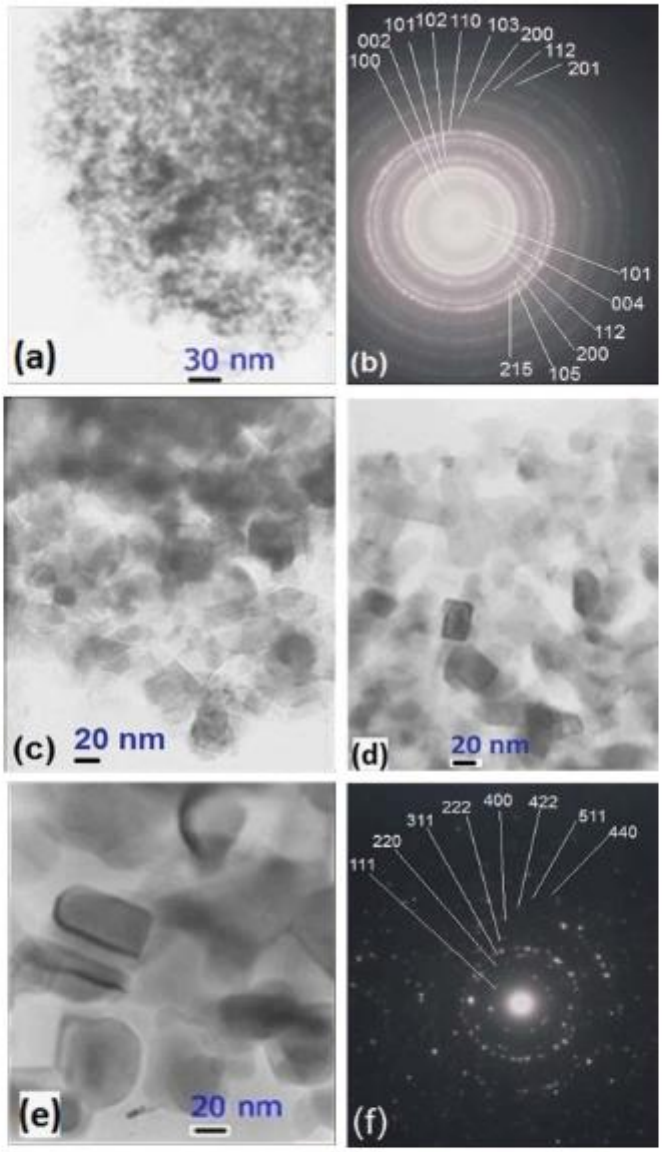

Fig. 3. TEM images and SAED patterns of (a, b) Bnon, (c, d) B500 and (e, f) B700.

regions to surfaces of composited nanograins to promote photocatalysis. The higher photocatalytic activity of ZnO/TiO_2 nanocomposites was controlled by the role of ZnO on the surface of TiO_2 nanoparticles (Fig. 5), relating to the diffusion of electrons and holes in conduction and valence bands (CB, VB) with different energy levels of the couples. There are a number of p–n junctions containing in the ZnO/TiO_2 nanocomposites. At equilibrium, an electric field formed inside, which led the negative and positive charges to be in the p-type ZnO and n-type TiO_2, respectively. Furthermore, the photogenerated electrons in the CB of ZnO diffused into the CB of TiO_2. Concurrently, the photogenerated holes in the VB of TiO_2 diffused into the VB of ZnO. This efficient charged separation increases lifetime of the charged carriers and enhances the efficiency of the interfacial-charged diffusion process [3,10]. Holes combined with H_2O to form $^{\bullet}H$ and $^{\bullet}OH$ radicals. Concurrently, electrons diffused to the adsorbed O_2 to

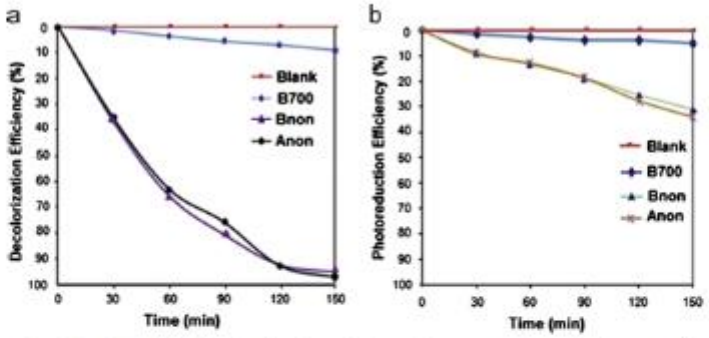

Fig. 4. (a) Photodegradation of MB and (b) photoreduction of $(Cr_2O_7)^{2-}$ by ZnO/TiO_2 nanocomposites and Zn_2TiO_4 comparing to the Blanks.

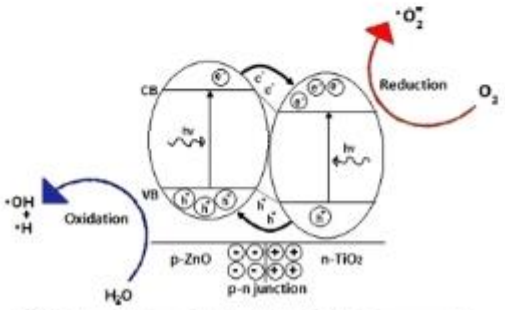

Fig. 5. Schematic diagram for photocatalysis of ZnO/TiO_2 nanocomposites.

form activated $\cdot O_2^-$ with subsequent transforming of water molecules into hydroxyl radicals. These oxidative species could effectively break down toxic organic substances back into original chemical forms of CO_2 and H_2O creating a cleaner and safer environment [11]. If the processes were not possible, electron–hole pairs would recombine together to generate heat inside or on surfaces of the composites.

In case of photoreduction of $(Cr_2O_7)^{2-}$ ions (Fig. 4b), both Anon and Bnon nanocomposites indicated the highest Cr(VI) reduction caused by the diffusion of electrons and holes at the ZnO/TiO_2 interfaces, and Cr(VI) combined with the photogenerated electrons to form Cr(III). The enhanced activity for Cr(VI) reduction was influenced by the difference of VB and CB energy levels of ZnO and TiO_2 to promote charged separation and to inhibit electron–hole recombination. The reduction could be inhibited by the formation of new electron–hole recombination centers, high temperature calcination to enlarge the particles and particle aggregation [11], including phase transformation.

4. Conclusions

A number of ZnO/TiO_2 nanocomposited particles were successfully synthesized by a microwave radiation through an aqueous solution containing $Zn(NO_3)_2 \cdot 6H_2O$ and $C_4K_2O_9Ti \cdot 2H_2O$ at the pH 10, and the further transformation of the nanocomposites to Zn_2TiO_4 nanocrystals by high temperature calcination. The nanocomposites showed the highest promising potential for water treatment with high efficiency.

Acknowledgments

We wish to thank the Thailand's Office of the Higher Education Commission for providing financial support through the National Research University Project and the Human Resource Development Project in Science Achievement Scholarship of Thailand, including the Graduate School of Chiang Mai University through the general support.

References

[1] Leary R, Westwood A. Carbon 2011;49:741–72.
[2] Tian J, Wang J, Dai J, Wang X, Yin Y. Surf Coat Technol 2009;204:723–30.
[3] Shifu C, Wei Z, Wei L, Sujuan Z. Appl Surf Sci 2008;255:2478–84.
[4] Ajimsha RS, Das AK, Singh BN, Misra P, Kukreja LM. Physica E 2010;42:1838–43.
[5] Huang H, Ruan X, Fang G, Li M, Zhao XZ. J Phys D 2007;40:7041–5.
[6] Wu GS, Zhuang YL, Lin ZQ, Yuan XY, Xie T, Zhang LD. Physica E 2006;31:5–8.
[7] Phuruangrat A, Thongtem T, Thongtem S. Mater Lett 2009;63:1224–6.
[8] Powder Diffract File, JCPDS-ICDD, 12 Campus Boulevard, Newtown Square, PA 19073-3273, USA; 2001.
[9] Stengl V, Bakardjieva S, Murafa N. Mater Chem Phys 2009;114:217–26.
[10] Liao DL, Badour CA, Liao BQ. J Photochem Photobiol A 2008;194:11–9.
[11] Ku Y, Huang YH, Chou YC. J Mol Catal A 2011;342–343:18–22.

Rare Met.
DOI 10.1007/s12598-015-0508-3

RARE METALS
www.editorialmanager.com/rmet

Photocatalytic activity of La-doped ZnO nanostructure materials synthesized by sonochemical method

Anukorn Phuruangrat*, Phattranit Dumrongrojthanath, Oranuch Yayapao, Jirapong Arin, Somchai Thongtem, Titipun Thongtem*

Received: 26 September 2014 / Revised: 26 December 2014 / Accepted: 21 April 2015

Abstract ZnO nanostructure materials doped with different La contents were synthesized by sonochemical method. The products were characterized by X-ray diffraction (XRD), scanning electron microscopy (SEM), transmission electron microscopy (TEM), Raman spectroscopy, and Fourier transform infrared spectroscopy (FTIR). In this research, XRD patterns of pure ZnO and La-doped ZnO are specified as hexagonal wurtzite ZnO structure with no detection of La_2O_3 phase. SEM and TEM characterization revealed the flower shape of pure ZnO built-up from petals of hexagonal prisms with hexagonal pyramid tips. Upon doping with La, the flower-shaped ZnO is broken into individual 1D prism-like nanorods. Photocatalytic activities of the as-synthesized products were determined by measuring the degradation of methylene blue (MB) under ultraviolet–visible (UV) light irradiation. Among them, the 2.0 mol% La-doped ZnO shows better photocatalytic properties than any other products.

Keywords Nanostructure materials; Sonochemical method; Photocatalysis

A. Phuruangrat*
Department of Materials Science and Technology, Faculty of Science, Prince of Songkla University, Hat Yai 90112, Thailand
e-mail: phuruangrat@gmail.com; phuruangrat@hotmail.com

P. Dumrongrojthanath, J. Arin, T. Thongtem*
Department of Chemistry, Faculty of Science, Chiang Mai University, Chiang Mai 50200, Thailand

O. Yayapao, S. Thongtem
Department of Physics and Materials Science, Faculty of Science, Chiang Mai University, Chiang Mai 50200, Thailand

S. Thongtem
Faculty of Science, Materials Science Research Center, Chiang Mai University, Chiang Mai 50200, Thailand

Published online: 18 June 2015

1 Introduction

Semiconductors doped with rare earth (RE) elements are technologically significant materials. They are promising materials used as optoelectronic devices and receive considerable interest for a number of applications, such as phosphors, display monitors, X-ray imaging, scintillators, optical communication, and fluorescence imaging due to their particular 4f–5d and 4f–4f electron transitions which are different from other elements. RE (III) ions are recognized as excellent candidates for luminescence centers of the doped semiconductors to tailor emission color, especially to develop red, green, and blue (RGB) radiations. To dope with RE^{3+} as luminescent centers, emission properties of semiconductors can be tailored toward selected wavelength of visible region, which is very important for a variety of applications, including multicolor emission of light-emitting devices [1–5].

Zinc oxide (ZnO) is one of the II–VI semiconducting materials. It has wide direct band gap of 3.37 eV and large exciton binding energy of 60 meV at room temperature. ZnO gets increasing attention due to its excellent electrical and optoelectronic properties. It can be used for a wide range of application, such as solar cells, gas sensors, optoelectronic devices, and surface acoustic waveguides [6–8]. Moreover, it exhibits better performance in degrading of various environmental pollutants: pesticides, detergents, dyes, and volatile organic compounds by transforming into carbon dioxide, water, and mineral acids under ultraviolet–visible (UV) light irradiation [6, 9]. ZnO doped with RE^{3+} is related to the surface states that favor energy transfer from ZnO to RE^{3+} and shows well-defined narrow optical transition between the spin orbit levels split under different manifold weak crystal fields [1, 10]. Various physical and chemical routes were used to synthesize

RE^{3+}-doped nanostructured material: electrochemical deposition [1], hydrothermal method [2, 4, 6], chemical vapor deposition (CVD) [3], sol–gel method [5, 10, 11], precipitation [9], solution combustion [12], and magnetron sputtering [13].

In this research, a facile route of sonochemical synthesis of La-doped ZnO nanostructure materials at low temperature was created. A possible mechanism on the growth of La-doped ZnO nanostructure was explained. In the end, the photocatalytic performance of pure ZnO and La-doped ZnO was investigated. It was found that La-doped ZnO showed better photocatalytic performance than pure ZnO.

2 Experimental

Zinc nitrate hexahydrate ($Zn(NO_3)_2{\cdot}6H_2O$) as zinc source, lanthanum nitrate hexahydrate ($La(NO_3)_3{\cdot}6H_2O$) as lanthanum source, and sodium hydroxide (NaOH) were used without further purification.

To synthesize 0 mol%, 0.4 mol%, 1.0 mol%, and 2.0 mol% La-doped ZnO, 0.005 mol ($Zn(NO_3)_2{\cdot}6H_2O$ and 0, 0.4, 1.0, and 2.0 mol% $La(NO_3)_3{\cdot}6H_2O$ were dissolved in 100-ml deionized water under continuous stirring until complete dissolution. Subsequently, 3 $mol{\cdot}L^{-1}$ NaOH solution was slowly dropped into these solutions until their pH reached 10 and the solutions became colorless. Each solution was agitated by an ultrasonic wave of Bandelin Sonorex Super RK 102 H at a frequency of 35 kHz for 5 h. The as-synthesized precipitates were separated by filtration and washed with water and ethanol several times. All the products were dried and collected for further characterization.

The products were characterized by X-ray diffraction (XRD) by a Philips X'Pert MPD X-ray diffractometer equipped with Cu Kα radiation over a range of 15°–60° using a scanning rate of 0.02 $(°){\cdot}s^{-1}$. The morphologies and elemental component were recorded by field emission scanning electron microscopy (FE-SEM) carried out using a JEOL JSM 6335F SEM at 20 kV and an energy-dispersive X-ray spectroscopy (EDX) analyzer. Transmission electron microscopic (TEM) images were taken on a JEOL JEM 2010 TEM with an acceleration voltage of 200 kV. The vibration modes were determined by Fourier transform infrared (FTIR) spectroscopy and Raman spectroscopy. The FTIR spectra were recorded on a PerkinElmer RX spectrometer with KBr as a diluting agent and operated in the wave number range of 400–4000 cm^{-1} with 4 cm^{-1} resolution. Raman spectroscopy (HORIBA Jobin–Yvon T64000) was operated using 30-mW and 632.8-nm wavelength Helium–Neon red laser.

Photocatalytic activities of the as-synthesized products were determined by specifying the degradation of methylene blue (MB) in aqueous solutions under a visible radiation of UV lamp. The 150 mg photocatalyst was suspended in a 150 ml of 1×10^{-5} $mol{\cdot}L^{-1}$ MB aqueous solution, which was magnetically stirred for 30 min in the dark to establish an adsorption–desorption equilibrium of MB on surface of the photocatalyst. The UV lamp was turned on to initiate photocatalysis. The solution was analyzed by ultraviolet-visible spectroscopy (UV–Vis, PerkinElmer Lambda 25 spectrometer) with λ_{max} of 664 nm. Decolorization efficiency was calculated using:

$$\text{Decolorization efficiency} = \frac{C_0 - C_t}{C_0} \times 100\,\% \quad (1)$$

where C_0 is the initial concentration of MB and C_t is the concentration of MB after UV irradiation for the length of time (t).

3 Results and discussion

Figure 1a shows XRD patterns of La-doped ZnO with different lanthanum contents. XRD pattern of the as-synthesized ZnO product can be indexed to hexagonal wurtzite ZnO structure corresponding to the database of JCPDS No. 36-1451. When lanthanum was doped into ZnO matrix, diffraction peaks of the doped products are almost similar to those of undoped hexagonal ZnO crystal. Their crystalline structure remains unchanged, which indicates that La^{3+} uniformly disperses across the hexagonal ZnO matrix [4, 14]. Furthermore, positions of the three main diffraction peaks (Fig. 1b) evidently shift to the smaller Bragg angle with an increase in the concentration of La^{3+} from 0 mol% to 2.0 mol%. Possibly, the covalent radius of La^{3+} (0.106 nm) is larger than that of Zn^{2+} (0.06 nm) [2, 11, 13, 14]. In this research, the unit cell parameters of pure ZnO and La-doped ZnO are summarized in Table 1. They increase with the increase in La content, in accordance with the report of Anandan et al. [15]: the unit cell parameters of ZnO, 0.5 mol% La-doped ZnO, and 1.0 mol% La-doped ZnO are as follows: $a = 0.32480$, 0.32590, and 0.32670 nm, and $c = 0.52050$, 0.52170, and 0.52180 nm, respectively.

The products were diluted with potassium bromide in the ratio of 1:100 for FTIR analysis. Figure 2 shows FTIR spectra of 0 mol%–2.0 mol% La-doped ZnO products. The strong absorption bands at 426 and 565 cm^{-1} are attributed to the Zn–O stretching vibration of wurtzite hexagonal-type ZnO crystal [16, 17], belonging to the oxygen sublattice (E_{2H}) vibration and oxygen vacancies of wurtzite ZnO crystal, respectively [18]. The band at 1385 cm^{-1} is specified as hydrogen-related defects on surface of ZnO

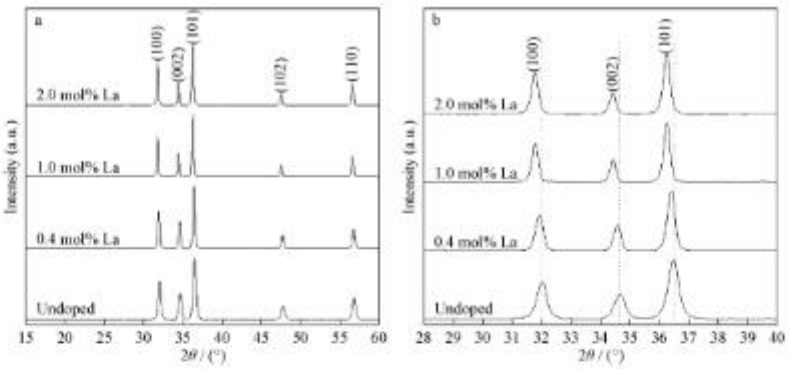

Fig. 1 XRD patterns of pure ZnO and La-doped ZnO over 2θ range of **a** 15°–60° and **b** 28°–40°

Table 1 Lattice parameters of present products

Products	Lattice parameter/nm	
	a	*c*
Pure ZnO	0.32456	0.52050
0.4 mol% La–ZnO	0.32536	0.52137
1.0 mol% La–ZnO	0.32695	0.52372
2.0 mol% La–ZnO	0.32698	0.52375

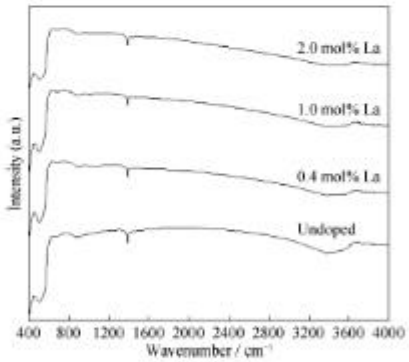

Fig. 2 FTIR spectra of pure ZnO and La-doped ZnO synthesized by sonochemical method

[19]. The broad absorption bands at 3013–3633 cm^{-1} are the O–H stretching vibration of adsorbed water on ZnO surface [16–18].

Figure 3 shows Raman spectra of the as-synthesized undoped and La-doped ZnO products. The polar optical branches of A_1 and E_1 are split into longitudinal and

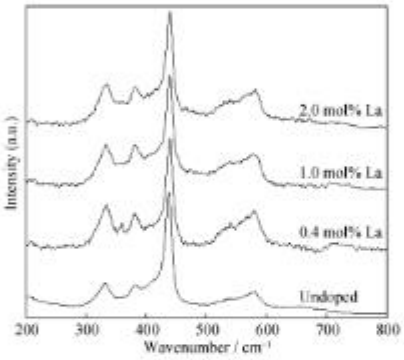

Fig. 3 Raman spectra of pure ZnO and La-doped ZnO synthesized by sonochemical method

transverse optical (LO and TO) components. The peak corresponding to ZnO nonpolar optical phonon high E_2 mode is detected at 437 cm^{-1} [6, 10, 11], including the A_1 symmetry with TO mode at 378 cm^{-1} [6, 19]. The peak at 329 cm^{-1} for ZnO corresponds to the E_{2H}–E_{2L} mode [7, 10]. The peak centering at 583 cm^{-1} is indexed as the E_1 symmetry with LO mode [6, 19]. In this research, Raman spectra of La-doped ZnO agree well with those of pure ZnO with a decrease in the intensity of the peaks. The peak of E_2 mode is significantly restricted due to the loading of lanthanum, which leads to the existence of ZnO lattice [6]. Compared to those of pure ZnO, the E_{2H} modes of La-doped ZnO are blueshifted from 437 to 441 cm^{-1}, with a decrease in the intensity [10, 11, 19]. The blueshift is attributed to the residual stress along the *c*-axis due to the lattice distortion [10, 11]. The E_{1L} peak centered at 580 cm^{-1} of La-doped ZnO products is the result of

impurities and the formation of defects such as oxygen vacancies and Zn interstitial atoms [7, 10].

Morphologies of the products were investigated by FE-SEM as shown in Fig. 4. SEM image of pure ZnO product shows uniform flower-shaped built-up of hexagonal prisms with hexagonal pyramid tips. The surface of the hexagonal prism petals of flower-like ZnO is very smooth. For each flower, several hexagonal pyramid ZnO petals are grown out of the same distinguished ZnO nucleation site through their base and formed flower-like morphology. The hexagonal pyramid petals of flower-like ZnO are broken into individual 1D prism by La doping. Upon doping with La up to 2.0 mol%, the product is transformed into a large number of ZnO nanorods. Furthermore, small nanoparticles of ZnO crystal are also detected. In addition, EDS was used to determine elemental constituents of La^{3+}/ZnO composites, which show signals of Zn at about 1.01, 8.63, and 9.57 keV, oxygen at about 0.53 keV, and La at about 0.84, 4.65, 5.04, and 5.40 keV.

Figures 5 and 6 show TEM images and SAED patterns of the pure ZnO and 2.0 mol% La-doped ZnO products. They are composed of homogenous nanorods with an average diameter of 15–25 nm. SAED patterns of pure ZnO and 2.0 mol% La-doped ZnO products taken from individual single nanorods of both show bright spots of electron diffraction which reveals single-crystalline nature of ZnO and La-doped ZnO nanorods with the electron beam pointing along the same [−110] zone axis. The SAED patterns can be indexed as the (110) plane which is parallel to the preferential growth along the [001] direction of ZnO and La-doped ZnO nanorods. In general, anisotropic growth direction of ZnO is determined by interfacial free energy as well as dissolution ability in water. The growth is also controlled by the relative growth velocity of different planes. Moreover, the polar faces with surface

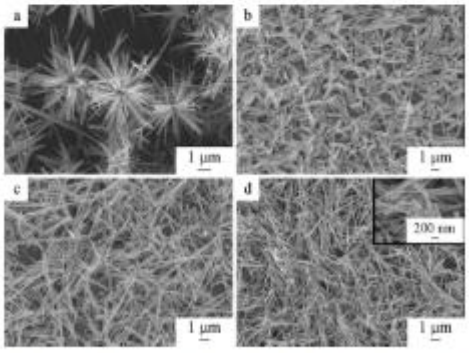

Fig. 4 SEM images of **a** pure ZnO, **b** 0.4 mol% La-doped ZnO, **c** 1.0 mol% La-doped ZnO, and **d** 2.0 mol% La-doped ZnO

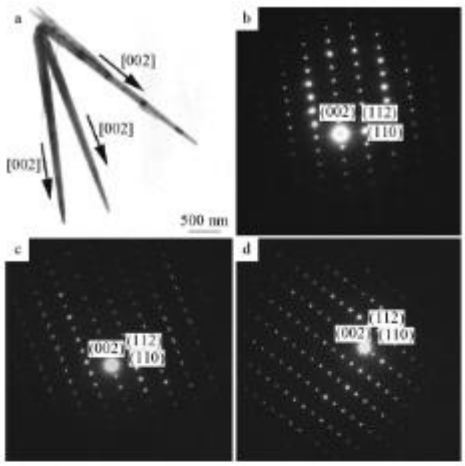

Fig. 5 TEM image **a** and SAED patterns **b**–**d** of undoped ZnO

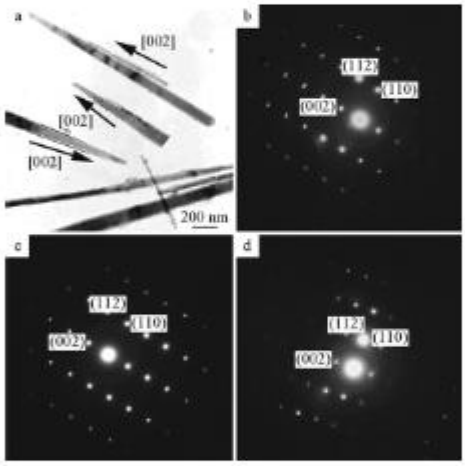

Fig. 6 TEM image **a** and SAED patterns **b**–**d** of 2.0 mol% La-doped ZnO

dipoles are less thermodynamically stable than those of nonpolar faces, which often undergo atomic rearrangement to minimize their surface energies and tend to grow more rapidly. Interestingly, morphologies of the as-synthesized 1D ZnO nanomaterials are fully consistent with the ideal hexagonal ZnO crystal model with the crystal growth velocity of various crystal facets of [0001] > [01–1–1] > [01–10] > [000–1] [20, 21]. Since the (0001) face has higher symmetry (C_{6v}) and specific surface free energy

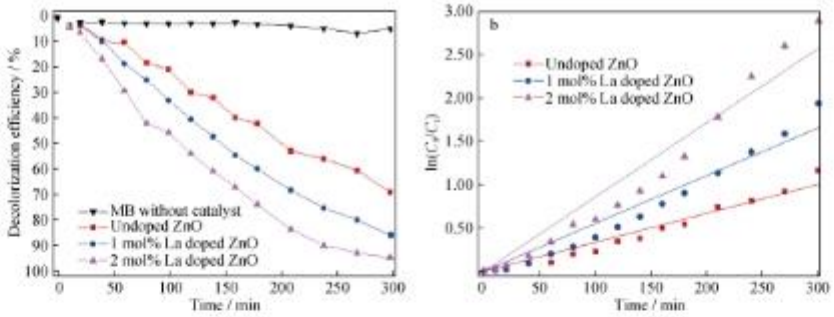

Fig. 7 Decolorization efficiency **a** and reaction kinetics **b** of present products

than any other faces [22], the growth rate along the [0001] direction is the highest, about twice of the [01–10] crystal direction, and the growth rate along the [01–1–1] is in the middle. Thus, the as-grown 1D ZnO nanomaterials grow along the [0001] direction bound with the six crystallographic {01–10} family planes [1, 20, 21].

Figure 7a shows the photocatalytic activities of pure ZnO, 1.0 mol% La-doped ZnO, and 2.0 mol% La-doped ZnO products. The degradation of MB is hardly detected without any catalyst under UV radiation. It is suggested that the photoinduced self-sensitized photolysis of MB could be neglected. The degradation efficiency of MB solution over pure ZnO is about 68.22 % within 300 min. However, the degradation efficiency is significantly improved under the same condition after La^{3+} was doped in the ZnO matrix. The photocatalytic efficiencies of 1.0 mol% La-doped ZnO and 2.0 mol% La-doped ZnO are enhanced to 85.38 % and 94.58 % within 300 min, respectively. To better understand the reaction kinetic of MB degradation catalyzed by pure ZnO and La-doped ZnO products, the relationship between $\ln(C_0/C_t)$ and the irradiation time for MB degradation was studied (Fig. 7b). The photocatalytic degradation curves fit well with the first-order linear equation. The 2.0 mol% La-doped ZnO exhibits the highest rate constant ($k = 8.66 \times 10^{-3}$ min^{-1}). It is approximately 2.6 times larger than that of pure ZnO ($k = 3.35 \times 10^{-3}$ min^{-1}).

Photocatalytic activity of the photocatalyst is mainly determined by several factors: morphology, Brunauer–Emmett–Teller (BET) surface area, crystalline facet, and dopant [6, 16, 18, 23–25]. Spherical ZnO has higher photocatalytic activity than flower-like ZnO, because it has rather higher specific surface area and pore volume than nanostructured flower shape [23]. The exposed crystalline face is noticeably different for ZnO particles with different morphologies: the more specific sites they have, the more their activities become. The unique ZnO nanodisks with high (0001) facet population and small surface area show better photocatalytic activity than other crystalline faces [24, 25]. In this work, single-crystalline nature of ZnO and La-doped ZnO nanorods is of preferential growth along the [001] direction. Therefore, La dopant has the influence on the photocatalytic efficiency of ZnO powder. The 2.0 mol% La-doped ZnO shows higher photocatalytic activity than other products, due to the concentration of oxygen defects on the surfaces of the doped nanocrystals [18].

4 Conclusion

In this research, La-doped ZnO was successfully synthesized via a sonochemical method. The experimental results demonstrate that the as-synthesized 2.0 mol% La-doped ZnO has an excellent photocatalytic activity than pure ZnO for degradation of MB under UV irradiation. This research may provide guidance for the treatment of organic pollutants.

Acknowledgments This work was financially supported by the National Research University Project for Chiang Mai University (CMU) from the Thailand's Office of the Higher Education Commission, Thailand.

References

[1] Li GR, Lu XH, Wang ZL, Yu XL, Tong YX. Controllable electrochemical synthesis of La^{3+}/ZnO hierarchical nanostructures and their optical and magnetic properties. Electrochim Acta. 2010;55(11):3687.

[2] Iqbal J, Liu X, Zhu H, Wu ZB, Zhang Y, Yu D, Yu R. Raman and highly ultraviolet red-shifted near band-edge properties of LaCe-co-doped ZnO nanoparticles. Acta Mater. 2009;57(16):4790.

[3] Lee SY, Shin YH, Kim Y, Kim S, Ju S. Thermal quenching behavior of emission bands in Eu-doped ZnS nanowires. J Lumin. 2011;131(11):1336.

[4] Wang M, Huang C, Huang Z, Guo W, Huang J, He H, Wang H, Cao Y, Liu Q, Liang J. Synthesis and photoluminescence of Eu-

doped ZnO microrods prepared by hydrothermal method. Opt Mater. 2009;31(10):1502.
[5] Ge C, Xie C, Hu M, Gui Y, Bai Z, Zeng D. Structural characteristics and UV-light enhanced gas sensitivity of La-doped ZnO nanoparticles. Mater Sci Eng B. 2007;141(1–2):43.
[6] Jia T, Wang W, Long F, Fu Z, Wang H, Zhang Q. Fabrication, characterization and photocatalytic activity of La-doped ZnO nanowires. J Alloys Compd. 2009;484(1–2):410.
[7] Thongtem T, Phuruangrat A, Thongtem S. Characterization of nanostructured ZnO produced by microwave irradiation. Ceram Int. 2010;36(1):257.
[8] Phuruangrat A, Thongtem T, Thongtem S. Microwave-assisted synthesis of ZnO nanostructure flowers. Mater Lett. 2009;63(13–14):1224.
[9] Anandan S, Vinu A, Lovely KLPS, Gokulakrishnan N, Srinivasu P, Mori T, Murugesan V, Sivamurugan V, Ariga K. Photocatalytic activity of La-doped ZnO for the degradation of monocrotophos in aqueous suspension. J Mol Catal A Chem. 2007;266:149–57.
[10] Yang J, Gao M, Yang L, Zhang Y, Lang J, Wang D, Wang Y, Liu H, Fan H. Low-temperature growth and optical properties of Ce-doped ZnO nanorods. Appl Surf Sci. 2008;255(1–2):2646.
[11] Chena JT, Wang J, Zhang F, Zhang GA, Wu ZG, Yan PX. The effect of La doping concentration on the properties of zinc oxide films prepared by the sol–gel method. J Cryst Growth. 2008;310(10):2627.
[12] Devi SKL, Kumar KS, Balakrishnan A. Rapid synthesis of pure and narrowly distributed Eu doped ZnO nanoparticles by solution combustion method. Mater Lett. 2011;65(1):35.
[13] Lan W, Liu Y, Zhang M, Wang B, Yan H, Wang Y. Structural and optical properties of La-doped ZnO films prepared by magnetron sputtering. Mater Lett. 2007;61(11–12):2262.
[14] Zhong M, Shan G, Li Y, Wang G, Liu Y. Synthesis and luminescence properties of Eu^{3+}-doped ZnO nanocrystals by a hydrothermal process. Mater Chem Phys. 2007;106(2–3):305.
[15] Anandan S, Vinu A, Mori T, Gokulakrishnan N, Srinivasu P, Murugesan V, Ariga K. Photocatalytic degradation of 2,4,6-trichlorophenol using lanthanum doped ZnO in aqueous suspension. Catal Commun. 2007;8(9):1377.
[16] Faisal M, Ismail AA, Ibrahim AA, Bouzid H, Al-Sayari SA. Highly efficient photocatalyst based on Ce doped ZnO nanorods: controllable synthesis and enhanced photocatalytic activity. Chem Eng J. 2013;229:225.
[17] Phuruangrat A, Thongtem T, Kuntalue B, Thongtem S. Microwave-assisted synthesis and characterization of rose-like and flower-like zinc oxide nano structures. J Ovonic Res. 2011;7(6):107.
[18] Yayapao O, Thongtem S, Phuruangrat A, Thongtem T. Sonochemical synthesis, photocatalysis and photonic properties of 3 % Ce-doped ZnO nanoneedles. Ceram Int. 2013;39(S1):S563.
[19] Yang L, Tang Y, Hu A, Chen X, Liang K, Zhang L. Raman scattering and luminescence study on arrays of ZnO doped with Tb^{3+}. Phys B. 2008;403(13–16):2230.
[20] Umar A, Al-Hajry A, Hahn YB, Kim DH. Rapid synthesis and dye-sensitized solar cell applications of hexagonal-shaped ZnO nanorods. Electrochim Acta. 2009;54(22):5358.
[21] Lee GH, Kim MS. Synthesis of bottle-shaped ZnO particles tthrough the oxidation of a mixture of Al-Zn-Au. Mater Trans. 2009;50(8):2121.
[22] Wei H, Wu Y, Lun N, Hu C. Hydrothermal synthesis and characterization of ZnO nanorods. Mater Sci Eng A. 2005;393(1–2):80.
[23] Kajbafvala A, Ghorbani H, Paravar A, Samberg JP, Kajbafvala E, Sadmezhaad SK. Effects of morphology on photocatalytic performance of zinc oxide nanostructures synthesized by rapid microwave irradiation methods. Superlattices Microstruct. 2012;51(4):512.
[24] Zeng JH, Jin BB, Wang YF. Facet enhanced photocatalytic effect with uniform single-crystalline zinc oxide nanodisks. Chem Phys Lett. 2009;472(1–3):90.
[25] Boppella R, Anjaneyulu K, Basak P, Manorama SV. Facile synthesis of face oriented ZnO crystals: tunable polar facets and shape induced enhanced photocatalytic performance. J Phys Chem C. 2013;117(9):4597.

Superlattices and Microstructures 67 (2014) 197–208

Contents lists available at ScienceDirect

Superlattices and Microstructures

journal homepage: www.elsevier.com/locate/superlattices

Synthesis, characterization and optical activity of La-doped $ZnWO_4$ nanorods by hydrothermal method

Jirapong Arin [a], Phattranit Dumrongrojthanath [a], Oranuch Yayapao [b], Anukorn Phuruangrat [c,*], Somchai Thongtem [b], Titipun Thongtem [a,*]

[a] Department of Chemistry, Faculty of Science, Chiang Mai University, Chiang Mai 50200, Thailand
[b] Department of Physics and Materials Science, Faculty of Science, Chiang Mai University, Chiang Mai 50200, Thailand
[c] Department of Materials Science and Technology, Faculty of Science, Prince of Songkla University, Hat Yai, Songkhla 90112, Thailand

ARTICLE INFO

Article history:
Received 15 December 2013
Accepted 26 December 2013
Available online 2 January 2014

Keywords:
La doped $ZnWO_4$
Hydrothermal
Nanorods

ABSTRACT

One-dimensional La doped $ZnWO_4$ nanostructures have been synthesized by hydrothermal method. The effect of various La contents doped $ZnWO_4$ samples on phase, morphologies and optical properties was investigated and characterized by X-ray diffraction (XRD), field scanning electron microscopy (FESEM), transmission electron microscopy (TEM), high resolution transmission electron microscopy (HRTEM), Raman and UV–visible spectroscopy, respectively. The results of XRD, SEM and SAED revealed that all products were one-dimensional monoclinic $ZnWO_4$ nanorods while doped La^{3+} constants into $ZnWO_4$ lattice. The observation of TEM and HRTEM showed that the obtained La^{3+} doped $ZnWO_4$ with different La constants were homogenous nanorods shapes with grow along [021] direction. The optical property result showed that La^{3+} doped $ZnWO_4$ is a red shifted absorption when comparing to pure $ZnWO_4$.

1. Introduction

In the past decade, $ZnWO_4$ has been wildly researched because of its interesting in chemical and physical properties such as laser hosts, magnetic, scintillated, luminescent and catalytic properties and potential applications such as optical fibers, scintillator materials, magnetic properties, and

* Corresponding authors. Tel.: +66 (0)74 288 374; fax: +66 (0)74 288 395.
E-mail address: phuruangrat@hotmail.com (A. Phuruangrat).

0749-6036/$ - see front matter © 2013 Elsevier Ltd. All rights reserved.
http://dx.doi.org/10.1016/j.spmi.2013.12.024

heterogeneous catalysis [1–3]. $ZnWO_4$ is a materials in wolframite structure and belongs monoclinic with C_{2h} point group symmetry and P2/c space group. There are two formula units per primitive cell, having the lattice parameters a = 4.69263 Å, b = 5.72129 Å, c = 4.92805 Å and β = 90.6321°. The presence of two non-equivalent oxygen atoms is responsible for three pairs of Zn–O and W–O bonds, having different lengths. Thus, both Zn and W ions are surrounded by six oxygen atoms coordination, forming distorted ZnO_6 and WO_6 octahedral coordination which either edge-sharing ZnO_6 octahedron or edge-sharing WO_6 octahedra are corner-linked by zigzag chains in parallel to [001] [1,2,4].

To increase the luminescence efficiency of phosphor, researchers have tried various approaches including modify phosphor particle size and surface morphology, adding conductive materials, mixing flux materials and doping a sensitizer to enhance excitation energy absorption and energy transfer to the activator [5]. Doping method is a suitable synthesis method to increase the optical efficiency of oxide phosphor, rare-earth (RE) with their particular 4f–5d and 4f–4f electronic transition was used due to their unique optical transitions happen between the spin orbit levels split under the different manifolds weak crystal field and promising applications in optoelectronic devices [6–9]. By doping with RE^{3+} ions, it improves the luminescence efficiency by energy transfer processes [10]. For example, Anandan et al. report a high photocatalytic activity in the degradation of organic contaminants of La-doped TiO_2 due to the suppression of electron–hole recombination, large content of oxygen vacancies, and strong absorption of OH^- ions on the surface of the catalyst [11]. Jia et al. shows a strong emission peak centering at around 405 nm of La-doped ZnO which exhibited a red shift compared with the near band emission of pure ZnO because the incorporation of La^{3+} ions [12]. Here, we report one-dimensional La doped $ZnWO_4$ with differences La contents nanostructures by hydrothermal method. The effects of La doping on the structural and optical properties of $ZnWO_4$ were also investigated and discussed in detail.

2. Experimental procedure

All the chemicals used in the experiment, including zinc nitrate hexahydrate ($Zn(NO_3)_2{\cdot}6H_2O$), lanthanum nitrate hexahydrate ($La(NO_3)_3{\cdot}6H_2O$), sodium tungstate dihydrate ($Na_2WO_4{\cdot}2H_2O$) were used as zinc, lanthanum, tungsten sources, respectively are of analytic grade reagents without further purification.

In a typical procedure, the mixture containing 0.005 mol $Zn(NO_3)_2{\cdot}6H_2O$ and different amount of $La(NO_3)_3{\cdot}6H_2O$ (0.2, 0.4, 0.6, 1.0 and 2.0 wt%) was dissolved into 60 ml deionized water under rigorous stirring for 30 min. Then, 0.005 mol $Na_2WO_4{\cdot}2H_2O$ in 20 ml deionized water was added and the mixture solution was transferred into a Teflon lined steel autoclave of 100 ml, and the autoclave was heated at 180 °C for 24 h. Afterward, the autoclave was cooled to room temperature gradually. The white precipitate was washed with ethanol and distilled water three times. Then, it was dried at 80 °C for 12 h.

The products were characterized by X-ray diffraction (XRD) on a Philips, XPert MPD X-ray diffractometer equipped with Cu Kα radiation over a range from 10° to 60°. The scanning electron microscopy (SEM) images were carried out using a JEOL JSM-6335F field emission scanning electron microscopy (FESEM). Transmission electron microscopy (TEM) and high-resolution field emission transmission electron microscope (HRTEM) images and selected area electron diffraction (SAED) pattern were taken on a JEOL, JEM-2010 transmission electron microscopy with an acceleration voltage of 200 kV. Fourier transform infrared spectra (FT-IR) were recorded on a Bruker Tensor 27 FT-IR spectrometer with a KBr disk. Raman spectra were recorded on HORIBA JOBIN YVON T64000 Raman spectrometer with 50 mW and 514.5 nm wavelength Ar laser. UV–visible absorption spectra were recorded on a PerkinElmer, Lambda 25 UV–visible spectroscopy in wavelength range 200–800 nm.

3. Results and discussion

The phase structure of the products were examined by XRD. Fig. 1 shows XRD patterns of as-prepared pure $ZnWO_4$ and La-doped $ZnWO_4$ samples. For undoped $ZnWO_4$, all diffraction peaks can be readily indexed to the pure monoclinic $ZnWO_4$ structure with space group of P2/c and comprises

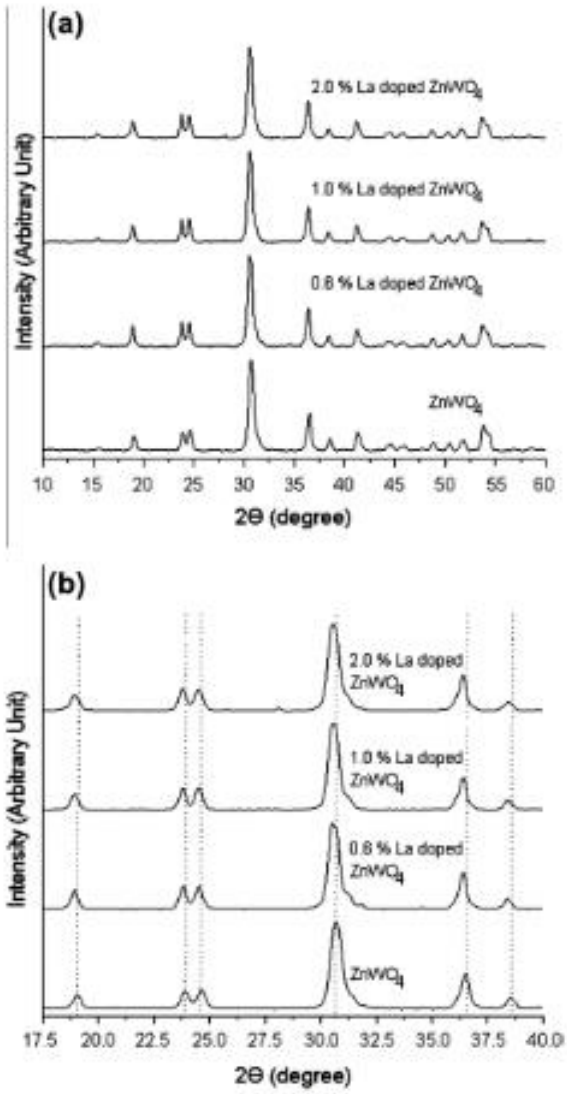

Fig. 1. XRD pattern of as-prepared 0–2% La doped $ZnWO_4$ samples synthesized by hydrothermal method.

infinite zigzag chains, running parallel to [001], of either edge-sharing ZnO_6 octahedron or edge-sharing WO_6 octahedra [1,2,14] which was in good agreement with JCPDS No. 15-0774 [13]. For La-doped $ZnWO_4$, they are still indexed the $ZnWO_4$ and no detected diffraction peaks of La_2WO_6, La_2O_3 or other impurity phases in La-doped $ZnWO_4$ samples. It indicated that the existence of La^{3+} did not significantly influence the phase and crystallization of the products and suggested that La^{3+} ions would uniformly substitute into the Zn^{2+} sites or interstitial sites in $ZnWO_4$ lattice. Fig. 1b of La-doped $ZnWO_4$ with compared to the pure $ZnWO_4$ in 2θ = 17.5–40°, it can be seen that all peaks were slightly shifted

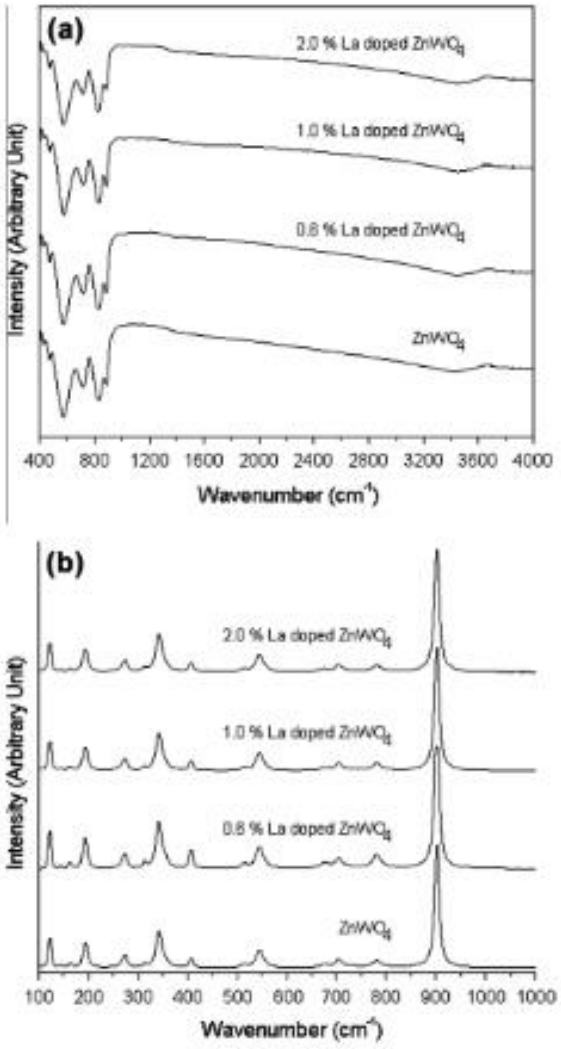

Fig. 2. FTIR and Raman spectra of 0–2% La doped $ZnWO_4$.

towards smaller diffraction angle. They suggested that the larger La^{3+} substitutes the smaller Zn^{2+} site partly so that the slightly shifting peak towards smaller diffraction angle. The ionic radius of La^{3+} (1.06 Å) is slightly larger than that of Zn^{2+} (0.74 Å), but much larger than that of W^{6+} (0.62 Å) in 6-fold coordination [15–17], so La^{3+} prefers to locating in Zn^{2+} sites without inversion center. As the amount of La^{3+} increases, it is observed that the corresponding XRD peaks move to lower degree according to previous reports which confirm that La^{3+} ions are inserted in $ZnWO_4$ lattice cell [11,12,15–19].

FTIR spectra of the La-doped $ZnWO_4$ samples with various concentration of La present in Fig. 2a. The products were mixed and diluted 10 times with potassium bromide (KBr). The background

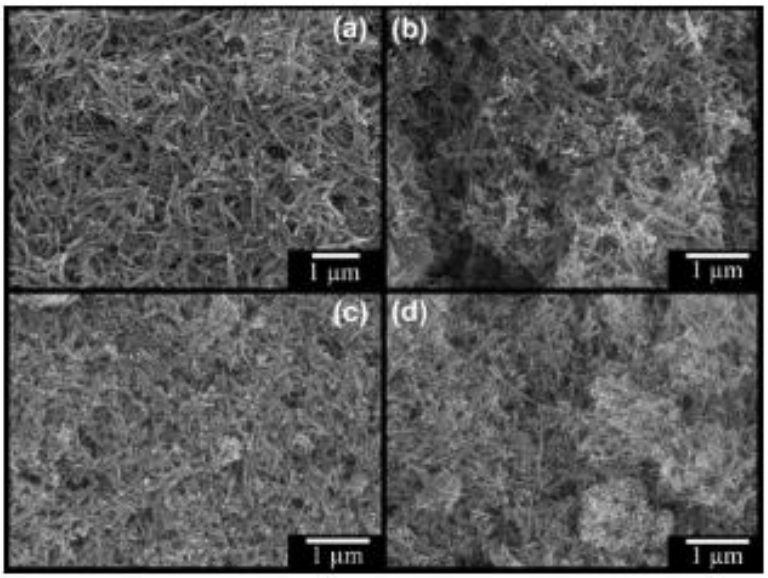

Fig. 3. SEM images of (a) 0%, (b) 0.4%, (c) 1% and (d) 2% La doped $ZnWO_4$.

spectrum recorded using KBr was subtracted from the products spectrum. The $ZnWO_4$ samples show six main absorption bands at 430–1000 cm^{-1}. The absorption bands at 834 and 877 cm^{-1} can be due to the stretching modes of W–O in WO_6 octahedra. The bands at 610 and 532 cm^{-1} were due to symmetrical vibrations of bridge oxygen atoms of the Zn–O–W groups. The absorption bands at 473 and 430 cm^{-1} can be assigned to symmetric and asymmetric deformation modes of W–O bonds and Zn–O bonds in WO_6 and ZnO_6 octahedra, respectively [1,2,20,21]. These vibrations could be identified to the synthesized $ZnWO_4$. Obviously, the board bands in the 3400 cm^{-1} is assigned to the O–H vibrations of H_2O molecule. It is also evident that the prepared samples contain a significant amount of surface-adsorbed water and some structural water.

Raman spectra of wolframite $ZnWO_4$ has 36 lattice vibration modes as $\Gamma = 8A_g + 10B_g + 8A_u + 10B_u$ by group theory. Only 18 modes of $8A_g$ and $10B_g$ are Raman active while15 modes of $7A_u$ and $8B_u$ are infrared (IR) active, and 3 modes of $1A_u$ and $2B_u$ are acoustic vibrations. Raman vibration of monoclinic wolframite $ZnWO_4$ was referred to the incompressibility of WO_6 octahedrons with respect to the ZnO_6 octahedrons [2,22,23]. Raman spectra of the samples in the range 100–1000 cm^{-1} are shown in Fig. 2b. Their peaks were assigned to the stretches of the W–O bands. The peak at 900 cm^{-1} was interpreted as an antisymmetric bridging mode associated with the tungstate chain. The bands about 300 cm^{-1} were assigned to the modes of terminal WO_2 group. The W–O bonds of intermediate length are characteristic of bridging W–O bonds and are assigned to Raman mode stretching wavenumbers in the 700–1000 cm^{-1} [2,23–25].

The general morphologies of the as-prepared La-doped $ZnWO_4$ products are examined by scanning electron microscopy (SEM) and transmission electron microscopy (TEM) observation. Fig. 3 shows the SEM images of La-doped $ZnWO_4$ with difference La contents. As can be seen from Fig. 3a, it reveals that the as-synthesized pure $ZnWO_4$ product consists of uniform nanorods and no detection of other shapes. It can be seen that these nanorods have a uniform diameter of about 20 nm and lengths up to 0.5–1 μm. The La-doped $ZnWO_4$ samples can be found that the morphologies of sample (Fig. 3b–d) are almost different. They found that the length of nanorod was decreased when increased the content of La doping. Finally, the completely short nanorods were produced at 2% La-doped $ZnWO_4$. In

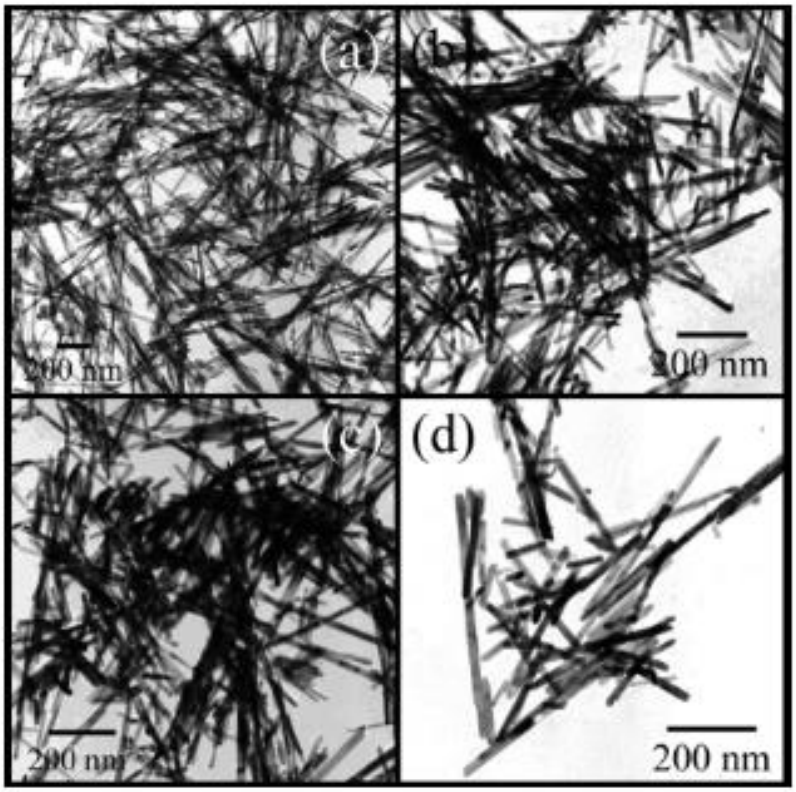

Fig. 4. TEM images of (a) 0%, (b) 0.4%, (c) 1% and (d) 2% La doped $ZnWO_4$.

addition, the EDS spectra show the chemical composition of sample which revealed the presence elementary components of Zn, W and O in $ZnWO_4$ and Zn, La, W and O in La-doped $ZnWO_4$.

The morphologies of the as-prepared La doped $ZnWO_4$ samples were further studied by TEM. Fig. 4 shows the morphologies of the as-synthesized samples were strongly dependent on La content doping. The $ZnWO_4$ without La doping as shown in Fig. 4a shows the uniform rod-shaped crystals and a majority of the crystals had exceeded 1500 nm in length. Fig. 4b–d shows the TEM image of La-doped $ZnWO_4$ for La = 0.4%, 1% and 2% by weight. Increasing of La content in $ZnWO_4$, the products are still one-dimensional $ZnWO_4$ nanostructures but not uniform in length. The products are mixture of short and long nanorod-shaped crystals can be seen. For 2% La-doped $ZnWO_4$ with two length ranges of 100–200 nm and 400–800 nm were observed.

To understand the preferential orientation growth, $ZnWO_4$ nanorods and 2% La-doped $ZnWO_4$ nanorods have been further studied using high resolution transmission electron microscope (HRTEM) and selected area electron diffraction (SAED) techniques and the results were shown in Figs. 5 and 6. The pure $ZnWO_4$ sample consists of unifrom nanorods with average width and length of 20 nm and >1500 nm (aspect ratio of >75). Each nanorod is straight and perfect over their entire lengths. The electron diffraction pattern of a single $ZnWO_4$ nanorod (Fig. 5c) obtained by focusing the electron beam perpendicular to the longitudinal axis presented in Fig. 5b. The SAED pattern revealed the product is a single-crystalline nature of the nanorods which can be index to (021), (121) and (100) planes with [01–2] as zone axis. So the nanorods grew preferentially along the [021] direction, which was parallel to the (100) face. The HRTEM image showed only one periodic fringe spacing which

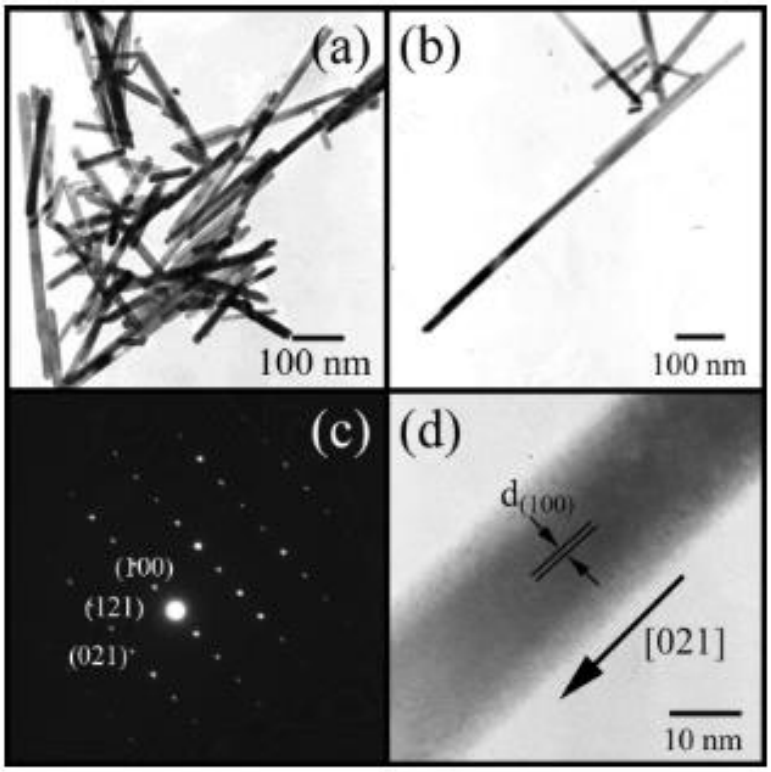

Fig. 5. TEM, HRTEM images and SAED pattern of $ZnWO_4$ sample.

confirmed that nanorod is a nanocrystalline structure. The lattice spacing of nanorod is along the longitudinal axis of the growth direction of nanorods which lattice spacing is 0.4674 nm which corresponded to the (100) plane of monoclinic $ZnWO_4$, as marked by an arrow in Fig. 5d. It confirms that the single $ZnWO_4$ nanorod is grow along the [021] direction.

Fig. 6 presents TEM and HRTEM images and SAED pattern of as-synthesized 2% La-doped $ZnWO_4$ sample. TEM image show that the product is rod-like in shape, which indicates the symmetrical growth of nanorods along a certain direction. It can be seen that the nanorods are about 10–25 nm in diameter and 60–600 nm in length with aspect ratio of 6–24. SAED pattern is essentially identified over the entire rod from individual $ZnWO_4$ nanorod in Fig. 6b, indicating the brightness sport pattern. It presents that product is a single-crystalline nature. SAED pattern revealed the (021), (121) and (100) plans in zone axis of [01–2] in accordance with the XRD result. Fig. 6d reveals the HRTEM image of 2% La-doped $ZnWO_4$. A lattice spacing of about 0.4673 nm can be observed, corresponding to the separation between the (100) planes of 2% La-doped $ZnWO_4$. It indicates that the growing plane and the growing direction of the nanorods are in the [021] direction, as marked by an arrow in Fig. 6d. Thus, both $ZnWO_4$ and 2% La-doped $ZnWO_4$ have the same growth direction along [021] which were confirmed by SAED and HRTEM results.

The optical absorption of the as-synthesized $ZnWO_4$ and La-doped $ZnWO_4$ nanorods was measured by UV–visible spectroscopy in wavelength of 200–800 nm in ethanol solution as shown in Fig. 7a. All samples show the spectra with two shoulder absorptions at around 240–260 nm and 280–290 nm

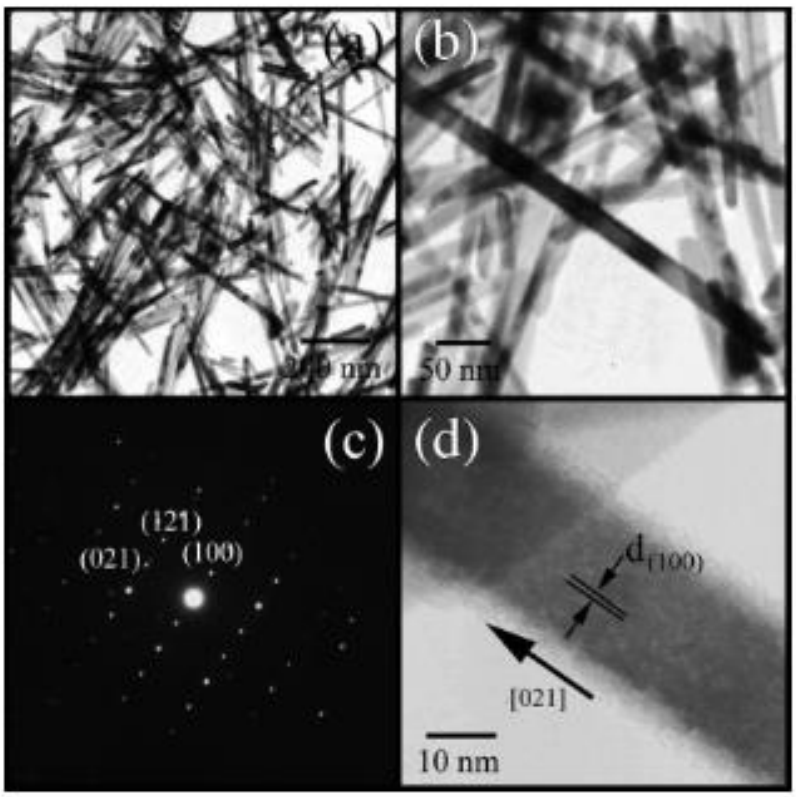

Fig. 6. TEM, HRTEM images and SAED pattern of as-synthesized 2% La-doped $ZnWO_4$ sample.

which assigned to be the intrinsic band gap transition. The band gaps of the as-synthesized $ZnWO_4$ nanorods were calculated by the below equation.

$$\alpha h\nu = (h\nu - E_g)^n \tag{1}$$

where α is the absorbance, h the Planck constant, ν the photon frequency, E_g the energy gap, and n the pure numbers associated with the different types of electronic transitions [1,14,17,18]. For n = 1/2, 2, 3/2 and 3, the transitions are the direct allowed, indirect allowed, direct forbidden, and indirect forbidden, respectively. The value of n for $ZnWO_4$ equals to 1/2 and its band gap was estimated to be 3.59, 3.53, 3.36, 3.24 and 3.11 eV for $ZnWO_4$, 0.2% La-doped $ZnWO_4$, 0.6% La-doped $ZnWO_4$, 1.0% La-doped $ZnWO_4$ and 2.0% La-doped $ZnWO_4$, respectively. It is worth to note that the La content in $ZnWO_4$ plays the role in decreasing the energy band gap.

4. Conclusions

In this research, 0–2% La doped $ZnWO_4$ nanorods have been synthesized by hydrothermal method. XRD patterns of pure $ZnWO_4$ and La doped $ZnWO_4$ samples are a wolframite monoclinic $ZnWO_4$ structure. Raman and FTIR spectra show a vibration of Zn–O, W–O and Zn–O–W in WO_6 and ZnO_6 octahedra. HRTEM image and SAED pattern confirmed that the nanorods grew preferentially along the [0 2 1]

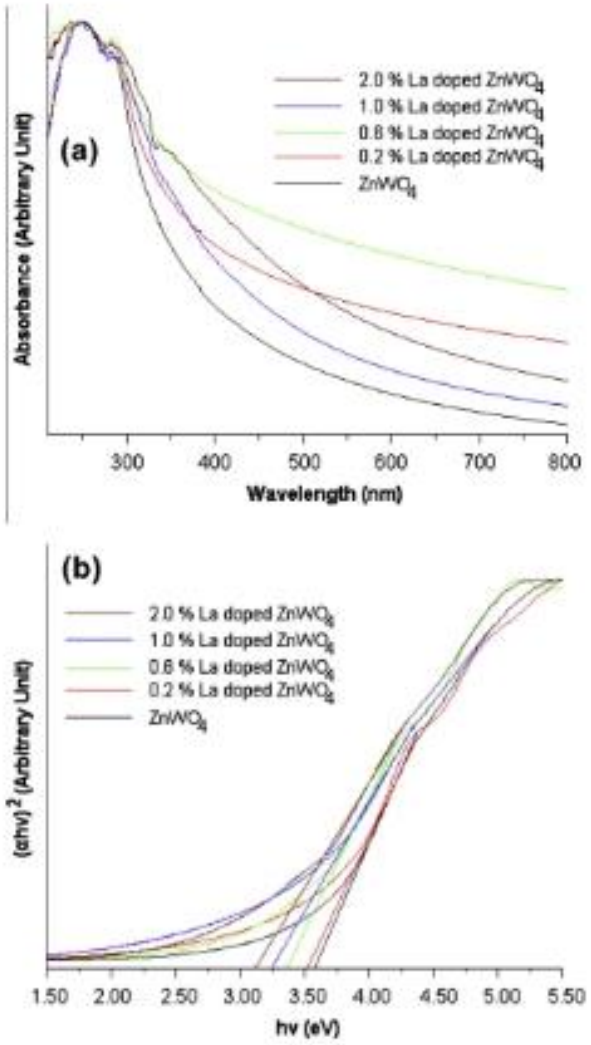

Fig. 7. (a) UV–visible spectra and (b) $(\alpha h\nu)^2$ vs $h\nu$ curves of products.

direction. The UV–visible spectra show the great absorbance in UV region assigned to be the intrinsic band gap transition.

Acknowledgements

We wish to thank the National Nanotechnology Center (NANOTEC), National Science and Technology Development Agency (NSTDA), for providing financial support through the project P-10-11345, and the Thailand's Office of the Higher Education Commission through the National Research University Project (NRU) for Chiang Mai University (CMU), and the Center for Innovation in Chemistry (PERCH-CIC), including the Graduate School of CMU through a general support.

References

[1] G. Huang, Y. Zhu, Synthesis and photocatalytic performance of $ZnWO_4$ catalyst, Mater. Sci. Eng. B 139 (2007) 201–208.
[2] P. Siriwong, T. Thongtem, A. Phuruangrat, S. Thongtem, Hydrothermal synthesis, characterization, and optical properties of wolframite $ZnWO_4$ nanorods, CrystEngComm 13 (2011) 1564–1569.
[3] W. Zhao, X. Song, G. Chen, S. Sun, One-step template-free synthesis of $ZnWO_4$ hollow clusters, J. Mater. Sci. 44 (2009) 3082–3087.
[4] A. Kalinko, A. Kuzmin, R.A. Evarestov, Ab initio study of the electronic and atomic structure of the wolframite-type $ZnWO_4$, Solid State Commun. 49 (2009) 425–428.
[5] S.H. Yang, F.S. Tsai, J.X. Chen, Characterizations of white-light $ZnWO_4$ phosphor prepared by blending complementary phosphor, J. Solid State Electrochem. 14 (2010) 937–943.
[6] J. Yang, M. Gao, L. Yang, Y. Zhang, J. Lang, D. Wang, Y. Wang, H. Liu, H. Fan, Low-temperature growth and optical properties of Ce-doped ZnO nanorods, Appl. Surf. Sci. 255 (2008) 2646–2650.
[7] W.E. Mahmoud, Synthesis and optical properties of Ce-doped ZnO hexagonal nanoplatelets, J. Cryst. Growth 312 (2010) 3075.
[8] C. Ge, C. Xie, M. Hu, Y. Gui, Z. Bai, D. Zeng, Structural characteristics and UV-light enhanced gas sensitivity of La-doped ZnO nanoparticles, Mater. Sci. Eng. B 141 (2007) 43–48.
[9] G.R. Li, X.H. Lu, Z.L. Wang, X.L. Yu, Y.X. Tong, Controllable electrochemical synthesis of La^{3+}/ZnO hierarchical nanostructures and their optical and magnetic properties, Electrochimica. Acta 55 (2010) 3687–3693.
[10] A. George, S.K. Sharma, S. Chawla, M.M. Malik, M.S. Qureshi, Detailed of X-ray diffraction and photoluminescence studies of Ce doped ZnO nanocrystals, J. Alloys Compd. 509 (2011) 5942–5948.
[11] J. Liqiang, S. Xiaojun, X. Baifu, W. Baiqi, C. Weimin, F. Honggang, The preparation and characterization of La doped TiO_2 nanoparticles and their photocatalytic activity, J. Solid State Chem. 177 (2004) 3375.
[12] T. Jia, W. Wang, F. Long, Z. Fu, H. Wang, Q. Zhang, Fabrication, characterization and photocatalytic activity of La-doped ZnO nanowires, J. Alloys Compd. 484 (2009) 410–415.
[13] Powder Diffract. File, JCPDS Internat. Centre Diffract. Data, PA 19073–3273, USA, 2001.
[14] M. Hojamberdiev, G. Zhu, Y. Xu, Template-free synthesis of $ZnWO_4$ powders via hydrothermal process in a wide pH range, Mater. Res. Bull. 45 (2010) 1934–1940.
[15] J. Iqbal, X. Liu, H. Zhu, Z.B. Wu, Y. Zhang, D. Yu, R. Yu, Raman and highly ultraviolet red-shifted near band-edge properties of LaCe-co-doped ZnO nanoparticles, Acta Mater. 57 (2009) 4790–4796.
[16] X.P. Chen, F. Xiao, S. Ye, X.Y. Huang, G.P. Dong, Q.Y. Zhang, $ZnWO_4$:Eu^{3+} nanorods: a potential tunable white light-emitting phosphors, J. Alloys Compd. 509 (2009) 1355.
[17] W. Lan, Y. Liu, M. Zhang, B. Wang, H. Yan, Y. Wang, Structural and optical properties of La-doped ZnO films prepared by magnetron sputtering, Mater. Lett. 61 (2007) 2262–2265.
[18] A. Kalinko, A. Kotlov, A. Kuzmin, V. Pankratov, A.I. Popov, L. Shirmane, Electronic excitations in $ZnWO_4$ and $Zn_xNi_{1-x}WO_4$ (x = 0.1–0.9) using VUV synchrotron radiation, Cent. Eur. J. Phys. 9 (2011) 432–437.
[19] M. Zhong, G. Shan, Y. Li, G. Wang, Y. Liu, Synthesis and luminescence properties of Eu^{3+}-doped ZnO nanocrystals by a hydrothermal process, Mater. Chem. Phys. 106 (2007) 305–309.
[20] G.B. Kumar, K. Sivaiah, S. Buddhudu, Synthesis and characterization of $ZnWO_4$ ceramic powder, Ceram. Int. 36 (2010) 199–202.
[21] R. Jia, Q. Wu, G. Zhang, Y. Ding, Preparation, structural and optical properties of $ZnWO_4$ and $CdWO_4$ nanofilms, J. Mater. Sci. 42 (2007) 4887–4891.
[22] D. Errandonea, F.J. Manjón, N. Garro, P. Rodríguez-Hernández, S. Radescu, A. Mujica, A. Muñoz, C.Y. Tu, Combined Raman scattering and ab initio investigation of pressure-induced structural phase transitions in the scintillator $ZnWO_4$, Phys. Rev. B 78 (2008) 054116.
[23] R. Jindal, M.M. Sinha, H.C. Gupta, Study of zone center phonons in wolframite $ZnWO_4$, Turk. J. Phys. 37 (2013) 107–112.
[24] H. Fu, C. Pan, L. Zhang, Y. Zhu, Synthesis, characterization and photocatalytic properties of nanosized Bi_2WO_6, $PbWO_4$ and $ZnWO_4$ catalysts, Mater. Res. Bull. 42 (2007) 696–706.
[25] T.T. Basiev, A.Ya. Karasik, A.A. Sobol, D.S. Chunaev, V.E. Shukshin, Spontaneous and stimulated Raman scattering in $ZnWO_4$ crystals, Quantum Electron. 41 (2011) 370–372.

Res Chem Intermed
DOI 10.1007/s11164-016-2818-y

Characterization of $ZnO–TiO_2$ and zinc titanate nanoparticles synthesized by hydrothermal process

Jirapong Arin[1,2] · Somchai Thongtem[3,4] · Anukorn Phuruangrat[5] · Titipun Thongtem[1]

Received: 16 August 2016 / Accepted: 21 November 2016

Abstract Solutions containing zinc nitrate hexahydrate ($Zn(NO_3)_2{\cdot}6H_2O$) and potassium titanium oxalate dihydrate ($C_4K_2O_9Ti{\cdot}2H_2O$) with different molar ratios of Zn:Ti at a pH of 10 were hydrothermally processed at 120, 160, and 200 °C to form ZnO–anatase, ZnO–anatase–rutile and ZnO–rutile nanocomposites. Upon subsequent calcination the precursors at high temperatures, $ZnTiO_3$, Zn_2TiO_4 , and $Zn_2Ti_3O_8$ nanoparticles were synthesized. X-ray diffraction (XRD), scanning electron microscopy (SEM), transmission electron microscopy (TEM), selected area electron diffraction (SAED), Fourier transform infrared (FTIR) spectroscopy, Raman spectrophotometry, and photoluminescence (PL) spectroscopy revealed the existence of nanocomposites and nanoparticles with strong emission at 386 nm for Zn_2TiO_4 and $Zn_2Ti_3O_8$ and at 370 nm for $ZnTiO_3$.

Keywords $ZnTiO_3$ · Zn_2TiO_4 · $Zn_2Ti_3O_8$ · Spectroscopy

✉ Anukorn Phuruangrat
phuruangrat@hotmail.com

✉ Titipun Thongtem
ttpthongtem@yahoo.com

[1] Department of Chemistry, Faculty of Science, Chiang Mai University, Chiang Mai 50200, Thailand

[2] The Graduate School, Chiang Mai University, Chiang Mai 50200, Thailand

[3] Department of Physics and Materials Science, Faculty of Science, Chiang Mai University, Chiang Mai 50200, Thailand

[4] Materials Science Research Center, Faculty of Science, Chiang Mai University, Chiang Mai 50200, Thailand

[5] Department of Materials Science and Technology, Faculty of Science, Prince of Songkla University, Hat Yai, Songkhla 90112, Thailand

Published online: 28 November 2016

Introduction

Size dependence of nanoparticles during solid–solid phase transition is one of the most interesting nanotechnologies because the nanoparticles can play an important role in bridging bulk materials (250–1000 nm), atomic/molecular structure (50–250 nm), and even quantum-size effect (<50 nm). Physical properties of bulk materials are constant, but nanosize-dependent properties are generally varied. Basing on the melting point of nanoparticles, the thermal behaviors are inverse size dependence in phase transition temperature due to the direct correlation of volume-surface ratio. For condensed form of fine powder, irregular particle size and shape can lead to non-uniform packing morphology and density. Thus, the properties of materials change as their size approaches nanoscale. The atoms on the surface of materials are the key step to improve functionality and are significant for industrial and military sectors [1–4].

Zinc titanate (ZTO) is a low-temperature calcining dielectric material. The ZnO–TiO_2 system contains Zn_2TiO_4 (zinc orthotitanate) with inverse spinel structure, $ZnTiO_3$ (zinc metatitanate) with hexagonal structure and cubic $Zn_2Ti_3O_8$ structure (zinc polytitanate). ZTO has been widely used as a catalyst and pigment in industries. It can be used as an efficient sorbent material for removal of multiple contaminants in high-efficiency energy conversion processes. Current technologies use a multistage process (expensive) for the removal of contaminations. ZTO is cheaper and more efficient in removing of contaminants from hot coal gases. Nanoscale ZTO is expected to achieve low-temperature sintering, which is a desired property of microwave dielectrics [5–12]. The degree of crystallinity of semiconducting titanate-type compounds showed difference photoluminescence (PL) phenomena. Previously, high crystalline titanate materials showed higher photoluminescence emission than amorphous materials. This effect has been widely studied for optical-electronic applications [13–16].

ZnO–TiO_2 nanoparticles with high surface area to volume ratio provide reduction of melting point of materials by reduction their size. This phenomenon is very interesting in nanomaterials, which are melted at a temperature hundreds of degrees lower than their bulks. Melting-point depression can create a large driving force for diffusion, especially at elevated temperature [17]. $ZnTiO_3$, Zn_2TiO_4 , and $Zn_2Ti_3O_8$ phases are ready to form because of their thermodynamic stability, precisely stoichiometric amount of ZnO–TiO_2 nanocomposites, and the effect of spinel structure. Previously, coarse particles require a large amount of energy to produce the titanate. Based on the ZnO–TiO_2 phase diagram, they require more than 820 °C, which can cause some competition reaction: decomposition of $ZnTiO_3$ into Zn_2TiO_4 + TiO_2 (rutile), $Zn_2Ti_3O_8$ into $ZnTiO_3$ + TiO_2 (rutile) and interfere the synthesis of pure phase [18–21].

$$Zn_2Ti_3O_8 \rightarrow 2ZnTiO_3 + TiO_2(\text{rutile}) \quad \text{when temperature} > 820\,^{\circ}\text{C}$$

$$2ZnTiO_3 \rightarrow Zn_2TiO_4 + TiO_2(\text{rutile}) \quad \text{when temperature} > 945\,^{\circ}\text{C}$$

The synthetic strategies are to synthesize $ZnTiO_3$, Zn_2TiO_4, and $Zn_2Ti_3O_8$ nanoparticles with high surface area to volume ratio. The process consumes short reaction time, rapid rate, and low temperature. The products were further characterized and the experimental results were investigated and discussed in this report.

Experiment

Preparation of $ZnO–TiO_2$ nanocomposites

Based on the chemical solution process, an analytical grade of 0.000, 0.100, and 0.200 mol zinc nitrate hexahydrate ($Zn(NO_3)_2{\cdot}6H_2O$) each was dissolved in 100 mL de-ionized water to form solutions to which ammonium hydroxide (NH_4OH) was slowly dropped until the pH was 10 and the solutions were transparent. Then 0.100 mol potassium titanium oxalate dihydrate ($C_4K_2O_9Ti{\cdot}2H_2O$) in 100 mL de-ionized water each was slowly mixed with the transparency solutions with keeping the pH at 10 throughout the process. These solutions were hydrothermally processed at different temperatures and lengths of time. Subsequently, the samples processed from different molar ratios were calcined at high temperatures and lengths of time, as summarized in Table 1.

Characterization

The as-prepared products were characterized by an X-ray diffractometer (XRD, SIEMENS D500) operating at 20 kV and 15 mA, a scanning electron microscope (SEM, JEOL JSM-6335F) operating at 15 kV with LaB_6 as a cathode for electron gun, a transmission electron microscope (TEM, JEOL JEM-2010), and selected area electron diffraction (SAED) operating at 200 kV, a Fourier transform infrared spectrometer (FTIR, Bruker Tensor 27) with KBr as a diluting agent operating in the range of 4000–400 cm^{-1}, a Raman spectrometer (T64000 HORIBA Jobin–Yvon) using a 50 mW and 514.5 nm wavelength Ar green laser, and a photoluminescence

Table 1 The samples prepared by different conditions

Samples	$Zn(NO_3)_2{\cdot}6H_2O$ (mole)	$C_4K_2O_9Ti{\cdot}2H_2O$ (mole)	Hydrothermal process		Calcination	
			T (°C)	t (h)	T (°C)	t (h)
S1	–	0.100	120	12	–	–
S2	0.200	0.100	120	12	700	3
S3	0.200	0.100	160	24	–	–
S4	0.100	0.100	200	48	750	3
S5	0.050 mol S2	0.100 mol S1	–	–	750	3

(PL) spectrometer (Perkin Elmer LS 50B) using a 250 nm excitation wavelength at room temperature.

Results and discussion

The nanocomposites were hydrothermally processed at different temperatures and lengths of time, and the XRD results are shown in Fig. 1. In this research, the products prepared from 0:1 to 2:1 molar ratios of Zn:Ti by hydrothermal process at

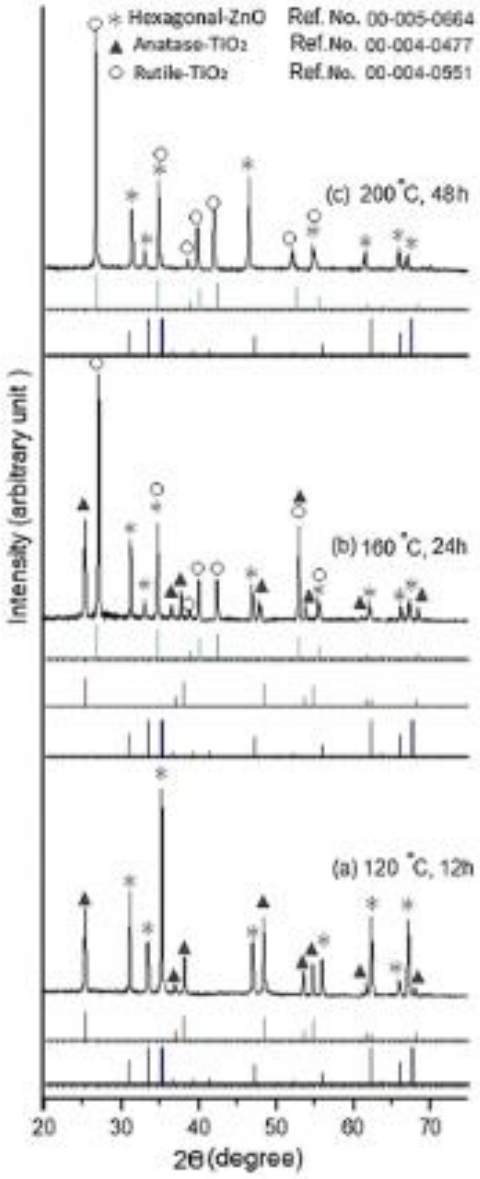

Fig. 1 XRD patterns of the product precursors synthesized by hydrothermal process at different temperatures and lengths of time: **a** ZnO–anatase, **b** ZnO–anatase–rutile, and **c** ZnO–rutile composites

120 °C for 12 h were composed of anatase, and wurtzite ZnO–anatase composites (JCPDS no 00-004-0477 for anatase and 00-005-0664 for ZnO) [22], respectively. Upon being hydrothermally processed, the mixture with 2:1 molar ratio of Zn:Ti at 160 °C for 24 h, additional rutile (JCPDS no 00-004-0551) [22] was also detected. For hydrothermal processing of the mixture with 1:1 molar ratio of Zn:Ti at 200 °C for 48 h, wurtzite ZnO–rutile composites were detected. At this condition, the whole anatase phase was transformed into the rutile phase.

The precursors were further calcined at different temperatures and lengths of time, as the XRD results show in Fig. 2. The hydrothermal sample processed from 1:1 molar ratio of Zn:Ti at 200 °C for 48 h and further calcined at 750 °C for 3 h was the $ZnTiO_3$ phase (JCPDS no. 00-026-1500) [22]. The sample hydrothermally processed from a 2:1 molar ratio of Zn:Ti at 120 °C for 12 h, and further calcined at 700 °C for 3 h leads to detect the Zn_2TiO_4 phase (JCPDS no. 00-019-1483) [22]. The mixture of as-prepared Zn_2TiO_4 and as-prepared anatase in a 1:2 molar ratio

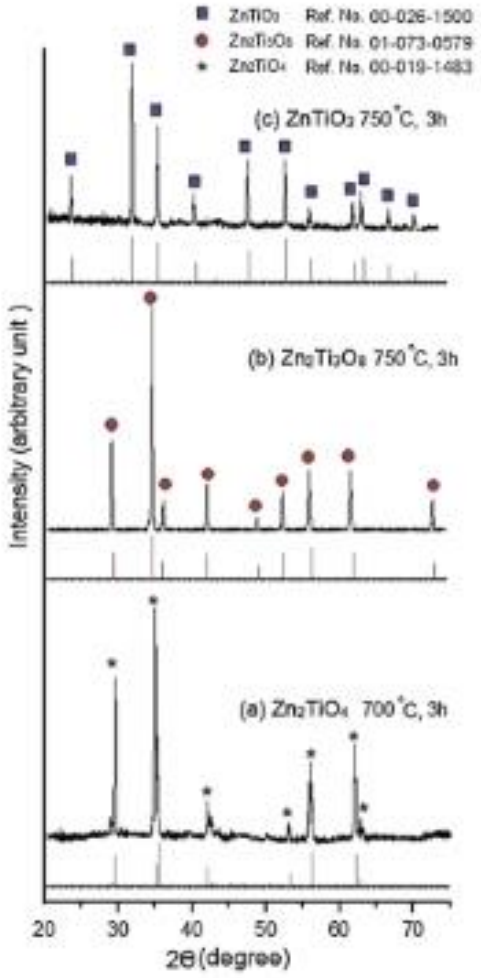

Fig. 2 XRD patterns of **a** Zn_2TiO_4, **b** $Zn_2Ti_3O_8$, and **c** $ZnTiO_3$

was calcined at 750 °C for 3 h, and the $Zn_2Ti_3O_8$ phase (JCPDS no. 01-073-0579) [22] was detected.

Upon dissolving of $C_4K_2O_9Ti{\cdot}2H_2O$ in water, the pH dropped down to 4.3. Generally, titanium ions exist in aqueous solution as hexaaqua coordination $[Ti(H_2O)_6]^{4+}$ complex [23]. When NH_4OH was slowly added to the solution, an O–H bond of $[Ti(H_2O)_6]^{4+}$ complex was broken by transforming into a hydroxide complex or the conjugate base of the $[Ti(H_2O)_6]^{4+}$ complex. The hydroxide complex withstood olation reaction, originated by releasing of one water molecule and combining with a neighboring complex. Under kinetic control of the olation reaction, bridging ligands start from *cis*-coordination reaction to form anatase structure. For thermodynamic control at high temperature, nuclei of the olation product starts from the *trans*-coordination reaction to form a rutile structure. Hydroxide ligands were bridged (denoted by μ) between two titanium atoms. During the process, ionization and condensation kept going even at high pH. In the end, anatase TiO_2 was obtained.

$$\left[Ti(H_2O)_6\right]^{4+} \rightarrow \left[Ti(H_2O)_5OH\right]^{3+} + H^+$$

$$\left[Ti(H_2O)_5OH\right]^{3+} + \left[Ti(H_2O)_6\right]^{4+} \rightarrow \left[Ti(H_2O)_5(\mu\text{-}OH)Ti(H_2O)_5\right]^{7+} + H_2O$$

$$\left[(Ti(H_2O)_5)_2(\mu\text{-}OH)\right]^{7+} \rightarrow \left[(Ti(H_2O)_5)_2(\mu\text{-}O)\right]^{6+} + H^+$$

$$\left[Ti(H_2O)_6\right]^{4+} \rightarrow TiO_2 + 4H_2O + 4H^+$$

In this research, anatase is considered a metastable phase due to the *cis*-coordination reaction under kinetic control at low temperature and short length of time. Rutile is a thermodynamic controlling phase at higher temperature and longer time. During processing, nuclei formed and grew to be crystals, originating from the order of TiO_6 octahedral units: zigzag for anatase and linear for rutile. The zigzag uses only the *cis*-coordination for crystal growth, but the linear requires the *trans*-coordination to bridge two octahedral units. The bridging structure is unstable under kinetic control process but the linear packing is the thermal stable structure due to the closest packing of TiO_6 octahedral units. The kinetic and thermodynamic models support the irreversible process of anatase. The anatase flavors to form specific titanate (Zn_2TiO_4 and $Zn_2Ti_3O_8$) because *cis*-transformation tends to form under cubic crystal system. The TiO_2, Zn_2TiO_4, $Zn_2Ti_3O_8$, and $ZnTiO_3$ phases consist of TiO_6 octahedrons connected through a common edge. The anatase and spinel-like structures (Zn_2TiO_4 and $Zn_2Ti_3O_8$) have common 3D frameworks. Moreover, rutile and $ZnTiO_3$ are composed of TiO_6 octahedral layers [23]. The formation of Zn_2TiO_4 and $Zn_2Ti_3O_8$ limited by the presence of anatase and $ZnTiO_3$ can form in the presence of rutile. The following decomposition reactions are

$$Zn_2Ti_3O_8 \rightarrow 2ZnTiO_3 + TiO_2(\text{rutile}), \quad \text{for } T > 820\,^{\circ}C$$

$$2ZnTiO_3 \rightarrow Zn_2TiO_4 + TiO_2(\text{rutile}), \quad \text{for } T > 945\,^{\circ}C$$

In this research, the ZTO can be synthesized at lower temperatures than 820 and 945 °C. By using the nanoprecursors, the calcination temperatures can be reduced to 700 °C for the synthesis of Zn_2TiO_4 and to 750 °C for the synthesis of $ZnTiO_3$ and $Zn_2Ti_3O_8$, as the XRD patterns shown in Fig. 2.

Figure 3 shows the morphologies and BET surface areas of $ZnO–TiO_2$ nanocomposites, $ZnTiO_3$, Zn_2TiO_4 , and $Zn_2Ti_3O_8$. ZnO–anatase nanocomposites synthesized at 120 °C for 12 h have the average diameter of <10 nm and surface area of 215.58 m^2/g that are appropriate for melting-point depression [23]. ZnO–anatase–rutile (151.62 m^2/g) and ZnO–rutile (148.06 m^2/g) nanocomposites became larger in sequence because they were synthesized at 160 °C for 24 h and at 200 °C for 48 h, respectively. Upon calcination the ZnO–anatase nanocomposites at 700 °C for 3 h, the Zn_2TiO_4 nanoparticles with the surface area of 52.49 m^2/g were produced. Different atoms in the materials diffused across the boundaries of the

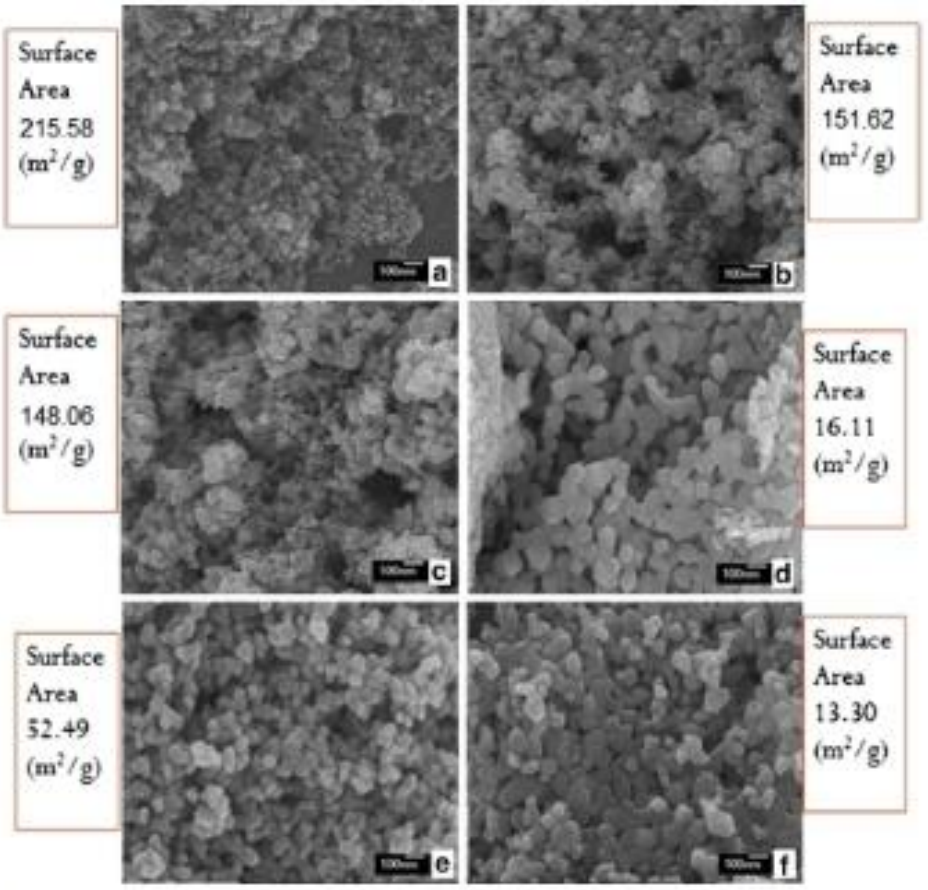

Fig. 3 SEM images and surface areas of the **a** ZnO–anatase, **b** ZnO–anatase–rutile, **c** ZnO–rutile, **d** $ZnTiO_3$, **e** Zn_2TiO_4, and **f** $Zn_2Ti_3O_8$ samples

particles. ZnO–anatase nanocomposites were chemically transformed into Zn_2TiO_4 nanoparticles with subsequent clustering together to form larger nanoparticles. During processing, counter diffusion of Zn^{2+} and Ti^{4+} could proceed as well. $ZnTiO_3$ nanoparticles were produced by calcination of ZnO–rutile nanocomposites with 1:1 molar ratio of Zn:Ti at 750 °C for 3 h. Their surface area was decreased to 16.11 m^2/g. Upon calcination the Zn_2TiO_4-anatase nanocomposites at 750 °C for 3 h, $Zn_2Ti_3O_8$ nanoparticles with surface area of 13.30 m^2/g were produced.

To understand further the nanostructure and phase of the products, ZnO–anatase, $ZnTiO_3$, Zn_2TiO_4 , and $Zn_2Ti_3O_8$ were characterized by TEM (Fig. 4) and SAED (Fig. 5). The TEM bright field image illustrates ZnO–anatase, which was composed of very tiny nanoparticles (<10 nm diameter) and the corresponding SAED pattern of ZnO–anatase nanocomposites. In general, the melting temperature (T_m) of nanoparticles is considered to be controlled by particle size. For nanoparticles, the surface area to volume ratio is large and the surface curvature is high. The melting temperature is size dependent and is the main objective to synthesize the

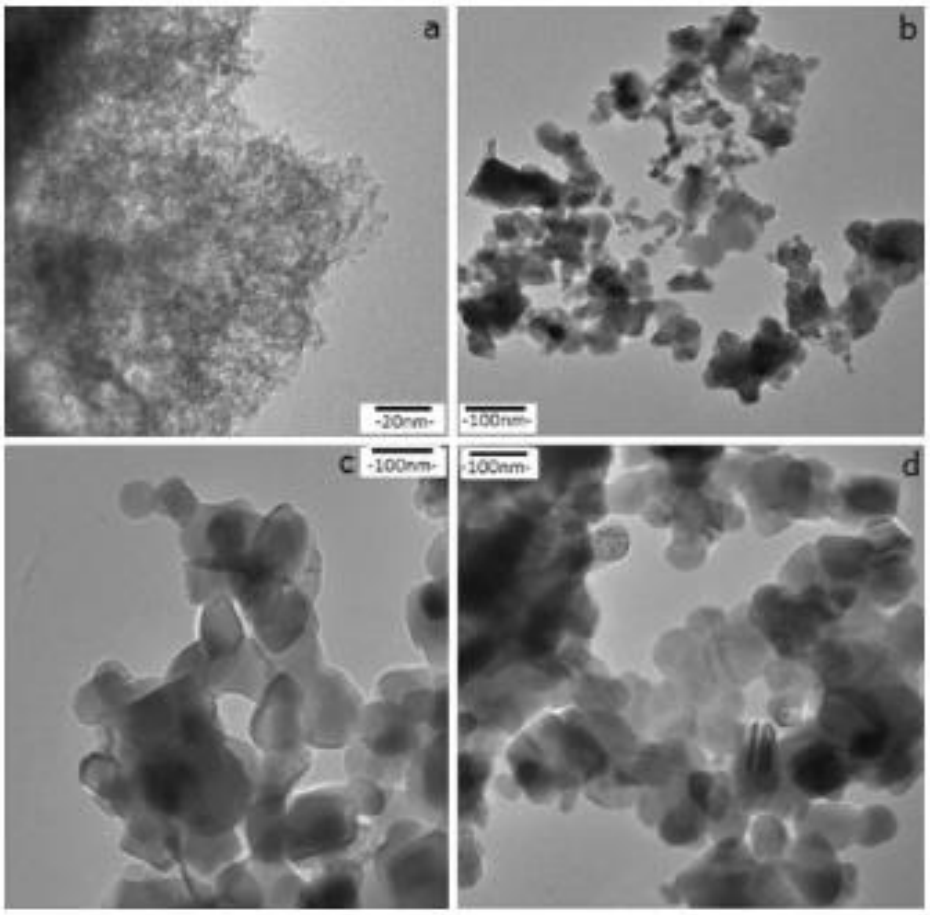

Fig. 4 TEM images of **a** ZnO–anatase, **b** $ZnTiO_3$, **c** Zn_2TiO_4 , and **d** $Zn_2Ti_3O_8$ nanoparticles

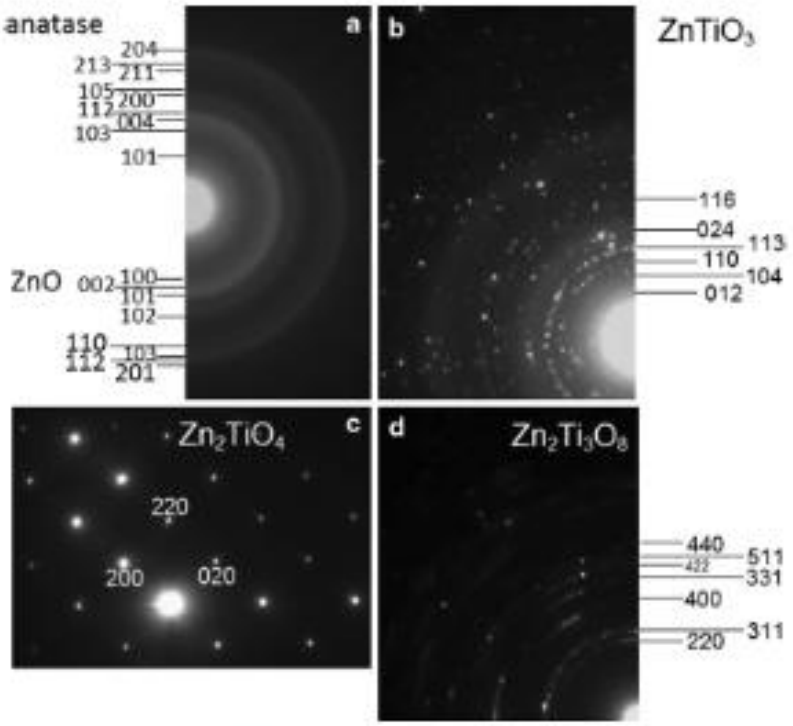

Fig. 5 SAED patterns of **a** ZnO–anatase, **b** $ZnTiO_3$, **c** Zn_2TiO_4 , and **d** $Zn_2Ti_3O_8$ nanoparticles

nanocomposites by low temperature calcination. The thermodynamic behavior has been explained and shown by an experimental procedure [24]. The SAED ring-pattern of $ZnTiO_3$ nanoparticles with the size range of 50–100 nm corresponding to the lattice fringe of the (012), (104), (110), (113), (024), and (116) planes is in accordance with the above XRD analysis. The present analysis shows the Zn_2TiO_4 fine nanoparticles with 40–80 nm average size and its corresponding SAED pattern with the [001] direction as zone axis. The $Zn_2Ti_3O_8$ sample was composed of a number of nanoparticles with 50–100 nm size range orientated in different directions, including the ring pattern containing the (220), (311), (400), (331), (422), (511), and (440) lattice planes.

Photoluminescence (PL) of the zinc titanate samples taken with an excitation wavelength of 250 nm is shown in Fig. 6. Both Zn_2TiO_4 and $Zn_2Ti_3O_8$ show strong PL emission at 386 nm and a weak band at 325 nm. Weak violet emission of Zn_2TiO_4 and $Zn_2Ti_3O_8$ was detected at 280 nm. In contrast, $ZnTiO_3$ shows a strong PL peak at 370 nm only. This detection belongs to hexagonal limonite type $ZnTiO_3$ [25]. Base on the SAED and TEM results, Zn_2TiO_4 is the only single perfect crystal with the highest degree of crystallinity. Thus, Zn_2TiO_4 has the highest PL intensity. The second PL intensity is $Zn_2Ti_3O_8$ because its formation reaction may cause a reduction in crystallinity, become more disordered polycrystal, and result in quenching of PL sensitivity. It was not the lowest intensity because single crystalline Zn_2TiO_4 used as the precursor is the best crystallinity. In contrast,

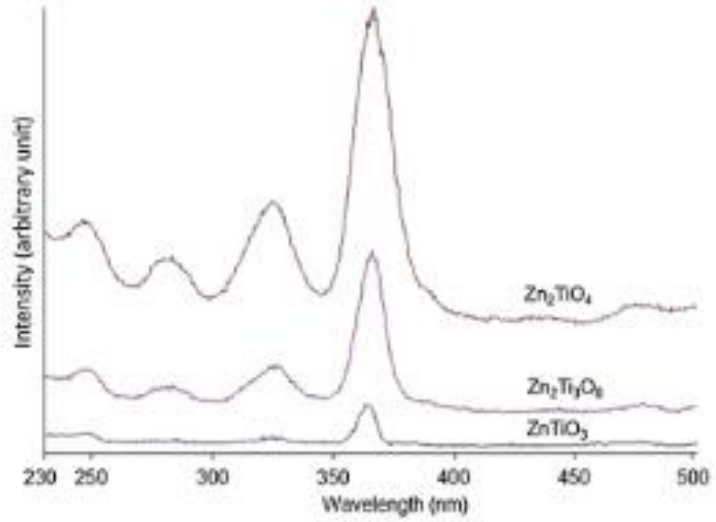

Fig. 6 Photoluminescence of $ZnTiO_3$, $Zn_2Ti_3O_8$, and Zn_2TiO_4

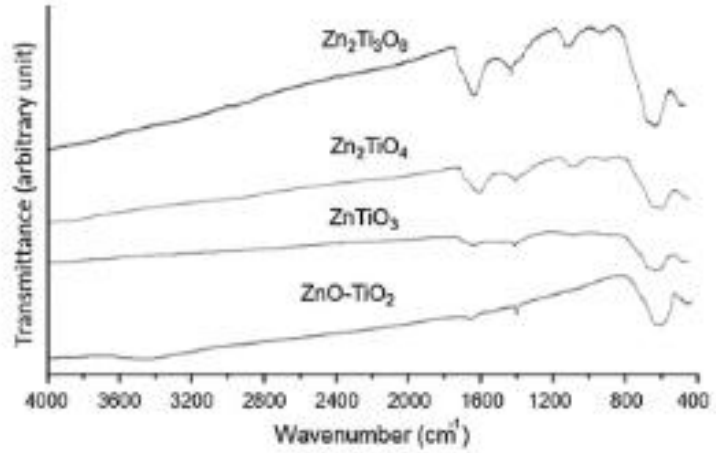

Fig. 7 FTIR spectra of ZnO–anatase, $ZnTiO_3$, Zn_2TiO_4, and $Zn_2Ti_3O_8$

$ZnTiO_3$ has the lowest PL intensity because the transformation of the stable rutile phase and ZnO to the titanate was very difficult comparing to that of the metastable anatase phase. This process can lead to real material system that always incorporate with disordered amorphous material. Different defects in the lattice can be caused by variation of the chemical constituents, as reported for the ZTO non-optical material [13, 14].

FTIR spectra of ZnO–anatase, $ZnTiO_3$, Zn_2TiO_4, and $Zn_2Ti_3O_8$ are shown in Fig. 7. Vibration modes of $[TiO_n]$ and Zn–O–Ti groups existing in different phases of the products were detected at 550–650 and 735 cm^{-1}, respectively. The wavenumber for Ti–O octahedral absorption of titanate increased with decrease in

Zn:Ti molar ratio. The ZnO_4 stretching vibration was detected at 400–500 cm^{-1}. Some residual oxalate groups were detected at 1400–1600 cm^{-1} [24].

Raman spectra of ZnO–anatase, Zn_2TiO_4, $Zn_2Ti_3O_8$, and $ZnTiO_3$ are shown in Fig. 8. ZnO has a wurtzite crystal structure with $P6_3mc$ space group. Its vibration modes are generally predicted by the optical theory group $A_1 + 2E_2 + E_1 + 2B_1$ [4]. The A_1 and E_1 phonon modes are both Raman and IR active, the E_2 mode is only Raman active, and the B_1 mode is forbidden. The strong and sharp peak at 435 cm^{-1} can be assigned to the high frequency of E_2, indicating that ZnO nanoparticles are good hexagonal oxide. The hexagonal ZnO revealed the Raman vibration at 320, 370, 405, and 575 cm^{-1}, assigned as the E_{2H}–E_{2L}, A_1(TO), E_1(TO), and E_1(LO) symmetrical phonon modes, respectively. The anatase was characterized to have five Raman active modes at about 153 cm^{-1} (E_g), 203 cm^{-1} (E_g), 390 cm^{-1} (B_{1g}), 515 cm^{-1} ($A_{1g} + B_{1g}$), and 605 cm^{-1} (E_{1g}). There are five Raman-active phonon modes ($A_{1g} + E_g + 3F_{2g}$) in the cubic spinel Zn_2TiO_4, as the results summarize in Table 2. The Raman vibrational modes at 257, 305, 380, 470, and 722 cm^{-1} were assigned as F_{2g}, E_g, F_{2g}, F_{2g}, and A_{1g} symmetrical phonon modes, respectively. $Zn_2Ti_3O_8$ has a cubic spinel structure with five Raman-active phonon modes ($A_{1g} + E_g + 3F_{2g}$). The vibrations were detected at 245, 310, 470, 520, and 718 cm^{-1} and were assigned as the F_{2g}, E_g, F_{2g}, F_{2g} , and A_{1g} symmetrical phonon modes, respectively. According to group theory, $ZnTiO_3$ (point group C3i) has 10 Raman active modes: $5A_g + 5E_g$. The Raman vibration of $ZnTiO_3$ was detected at 152, 188, 230, 262, 348, 403, 472, 486, 622, and 717 cm^{-1} and were specified as the E_g, A_g, E_g, A_g, A_g, E_g, E_g, A_g, E_g , and A_g symmetrical phonon modes, respectively.

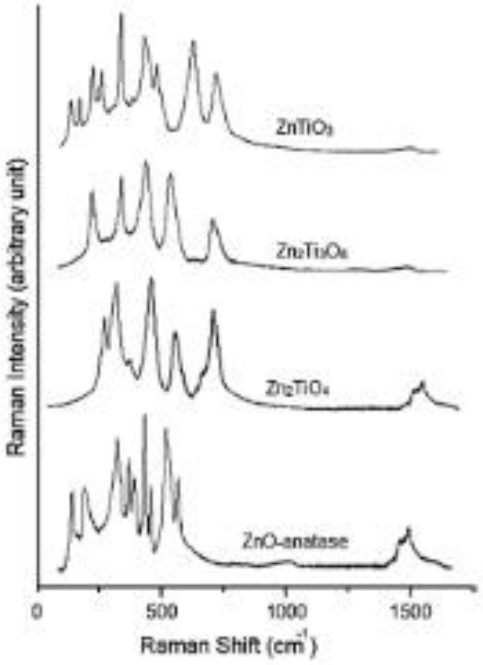

Fig. 8 Raman spectra of ZnO–anatase, Zn_2TiO_4, $Zn_2Ti_3O_8$, and $ZnTiO_3$

Table 2 Raman active modes of this work comparing to those of the previous reports [26–29]

Samples	Assignment	Previous reports (cm^{-1})	This work (cm^{-1})
ZnO	E_{2H}–E_{2L}	333 [26]	320
	A_1(TO)	379	370
	E_1(TO)	409	405
	E_{2H}	437	435
	E_1(LO)	583	575
TiO_2	E_g	143 [27]	153
	E_g	196	203
	B_{1g}	394	390
	$A_{1g} + B_{1g}$	515	515
	E_{1g}	637	605
Zn_2TiO_4	F_{2g}	265 [28]	257
	E_g	307	305
	F_{2g}	343	380
	F_{2g}	474	470
	A_{1g}	716	722
$ZnTiO_3$	E_g	146 [29]	152
	A_g	178	188
	E_g	233	230
	A_g	267	262
	A_g	345	348
	E_g	395	403
	E_g	472	472
	A_g	485	486
	E_g	620	622
	A_g	715	717
$Zn_2Ti_3O_8$	F_{2g}	N/A	245
	E_g		310
	F_{2g}		470
	F_{2g}		520
	A_{1g}		718

Conclusions

ZnO–TiO_2 (anatase/rutile) nanocomposites were successfully synthesized by a hydrothermal method. The samples were transformed into Zn_2TiO_4 nanoparticles by calcination of ZnO–anatase at 700 °C for 3 h and $ZnTiO_3$ nanoparticles by calcination of ZnO–rutile at 750 °C for 3 h. The $Zn_2Ti_3O_8$ sample was able to be synthesized by calcination of Zn_2TiO_4–anatase composites at 750 °C for 3 h. The Zn_2TiO_4 and $Zn_2Ti_3O_8$ samples show strong emission at 386 nm and $ZnTiO_3$ sample at 370 nm.

Acknowledgements We wish to thank Thailand's Office of the Higher Education Commission for providing financial support through the National Research University Project (NRU) for Chiang Mai University (CMU) and the Human Resource Development Project in Science Achievement Scholarship of Thailand, including the Graduate School of CMU through a general support.

References

1. S.H. Tolbert, A.P. Alivisatos, Science **265**, 373–376 (1994)
2. K. Jacobs, D. Zaziski, E.C. Scher, A.B. Herhold, A.P. Alivisatos, Science **293**, 1803–1806 (2001)
3. O. Yayapao, S. Thongtem, A. Phuruangrat, T. Thongtem, Ceram. Int. **39**, S563–S568 (2013)
4. A. Phuruangrat, S. Mad-ahin, O. Yayapao, S. Thongtem, T. Thongtem, Res. Chem. Intermed. **41**, 9757–9772 (2015)
5. S.F. Bartram, R.A. Slepetys, J. Am. Ceram. Soc. **44**, 493 (1961)
6. G.H. Pan, T. Hayakawa, M. Nogami, Z. Hao, X. Zhang, X. Qu, J. Zhang, RSC Adv. **5**, 88590 (2015)
7. R. Ramaseshan, S. Ramakrishna, J. Am. Ceram. Soc. **90**(6), 1836–1842 (2007)
8. Z. Ali, S. Ali, I. Ahmad, I. Khan, H.A.R. Aliabad, Phys. B **420**, 52–57 (2013)
9. L. Budigi, M.R. Nasina, K. Shaik, S. Amaravadi, J. Chem. Sci. **127**(3), 509–518 (2015)
10. P. Sirajudheen, J. Mater. Sci. Eng. **5**, 225 (2016)
11. H. Obayashi, Y. Sakurai, T. Gejo, J. Solid State Chem. **17**, 299–303 (1976)
12. T. Negas, T. Yeager, S. Bell, N. Coats, I. Minis, Am. Ceram. Soc. Bull. **72**, 80–89 (1993)
13. C.D. Pinheiro, E. Longo, E.R. Leite, F.M. Pontes, R. Magnani, J.A. Varela, P.S. Pizanni, T.M. Boschi, F. Lanciotti, Appl. Phys. A Mater. **77**, 81–85 (2003)
14. D.M.A. Melo, A. Cesar, A.E. Martinelli, Z.R. Silva, E.R. Leite, E. Longo, P.S. Pizanni, J. Solid State Chem. **177**, 670–674 (2004)
15. E. Orhan, F.M. Pontes, M.A. Santos, E.R. Leite, A. Beltran, J. Andres, T.M. Boschi, P.S. Pizani, J.A. Varela, C.A. Taft, E. Longo, J. Phys. Chem. B **108**, 9221–9227 (2004)
16. F.M. Pontes, C.D. Pinheiro, E. Longo, E.R. Leite, S.R. de Lazaro, R. Magnani, P.S. Pizani, T.M. Boschi, F. Lanciotti, J. Lumin. **104**, 175–185 (2003)
17. P. Buffat, J. Borel, Phys. Rev. **13**, 2287–2298 (1976)
18. U. Steinike, B. Wallis, Cryst. Res. Technol. **32**, 187 (1997)
19. H.T. Kim, Y. Kim, M. Valant, D. Suvorov, J. Am. Ceram. Soc. **84**, 1081 (2001)
20. F.H. Dulin, D.E. Rase, J. Am. Ceram. Soc. **43**, 125 (1960)
21. L. Helm, A.E. Merbach, Chem. Rev. **105**(6), 1923–1960 (2005)
22. Powder Diffract. File, JCPDS-ICDD, 12 Campus Boulevard, Newtown Square, PA 19073-3273, USA (2001)
23. N. Satoh, T. Nakashima, K. Yamamoto, Sci. Rep. **3**, 1959 (2013)
24. N. Nolan, M. Seery, S. Pillai, Chem. Mater. **23**(6), 1496–1504 (2011)
25. C. Alexsandra et al., J. Solid State Chem. **179**, 985–992 (2006)
26. R. Cuscó, E. Alarcón-Lladó, J. Ibáñez, L. Artús, J. Jiménez, B. Wang, M.J. Callahan, Phys. Rev. B **75**, 165202 (2007)
27. K.-R. Zhu, M.-S. Zhang, Q. Chen, Z. Yin, Phys. Lett. A **340**, 220–270 (2005)
28. T. Santhaveesuk, D. Wongratanaphisan, N. Mangkorntong, S. Choopun, Adv. Mater. Res. **55–57**, 641–644 (2008)
29. E.J. Baran, I.L. Botto, Z. Anorg, Allg. Chem. **448**, 188–192 (1979)

CIRRICULUM VITAE

Author's Name Mr. Jirapong Arin

Date/Year of Birth 19 July 1988

Place of Birth Bangkok, Thailand

Education 2007-2010 Bachelor of Science, Chemistry,
Chiang Mai University
2011-2012 Master of Science, Inorganic Chemistry,
Chiang Mai University

Publications

1) Jirapong Arin, Somchai Thongtem and Titipun Thongtem, "Single-step synthesis of ZnO/TiO_2 nanocomposites by microwave radiation and their photocatalytic activities", Material Letter, 96 (2013) 78-81.
2) Jirapong Arin, Somchai Thongtem and Titipun Thongtem et al., " Synthesis, characterization and optical activity of La-doped ZnWO 4 nanorods by hydrothermal method", *SUPERLATTICE MICROST*.67 (2014) 197-206.
3) A. Phuruangrat, J.Arin, S. Thongtem, T. Thongtem et al.," Synthesis, characterization and optical activity of La-doped ZnWO 4 nanorods by hydrothermal method", *Rare Metals*. 35 (2016) 390-395
4) J. Arin, A. Phuruangrat, S. Thongtem and T. Thongtem, "Characterization of ZnO–TiO2 and zinc titanate nanoparticles synthesized by hydrothermal process" Res. *Chem. Intermed. (Article in pressed)* (2016)

Experiences

1) Jirapong Arin, Somchai Thongtem and Titipun Thongtem," Synthesis of La-doped ZnO-TiO_2 Nanocomposites by cyclic-microwave radiation method and

Their Photocatalytic Activities" The Fourth International Conference on Science, Technology and Innovation for Sustainable Well-Being (STISWB IV), 10-12 August 2012, Thailand.